Evolutionary conservation of centriole rotational asymmetry in the human centrosome

Noémie Gaudin [1], Paula Martin Gil [1], Meriem Boumendjel [1], Dmitry Ershov [2,3], Catherine Pioche-Durieu [1], Manon Bouix [1], Quentin Delobelle [1], Lucia Maniscalco [1], Thanh Bich Ngan Phan [1], Vincent Heyer [4,5,6,7], Bernardo Reina-San-Martin [4,5,6,7] and Juliette Azimzadeh [1,8].

[1] Université de Paris, CNRS, Institut Jacques Monod, 75013, Paris, France.

[2] Image Analysis Hub, C2RT, Institut Pasteur, Paris, France.

[3] Hub de Bioinformatique et Biostatistique – Département Biologie Computationnelle, Institut Pasteur, USR 3756 CNRS, Paris, France.

[4] Institut de Génétique et de Biologie Moléculaire et Cellulaire (IGBMC), Illkirch, France.

[5] Institut National de la Santé et de la Recherche Médicale (INSERM), U1258, Illkirch, France.

[6] Centre National de la Recherche Scientifique (CNRS), UMR7104, Illkirch, France.

[7] Université de Strasbourg, Illkirch, France.

[8] Author for correspondence: juliette.azimzadeh@ijm.fr

Keywords: centriole, centrosome, LRRCC1, VFL1, C2CD3, Joubert syndrome, asymmetry.

Abbreviations:

DA: distal appendage; JBTS: Joubert syndrome; MCC: multiciliated cell; PCM: pericentriolar material; SAG: SMOOTHENED agonist; SMO: SMOOTHENED; TZ: transition zone.

Abstract

Centrioles are formed by microtubule triplets in a nine-fold symmetric arrangement. In flagellated protists and in animal multiciliated cells, accessory structures tethered to specific triplets render the centrioles rotationally asymmetric, a property that is key to cytoskeletal and cellular organization in these contexts. In contrast, centrioles within the centrosome of animal cells display no conspicuous rotational asymmetry. Here, we uncover rotationally asymmetric molecular features in human centrioles. Using ultrastructure expansion microscopy, we show that LRRCC1, the ortholog of a protein originally characterized in flagellate green algae, associates preferentially to two consecutive triplets in the distal lumen of human centrioles. LRRCC1 partially co-localizes and affects the recruitment of another distal component, C2CD3, which also has an asymmetric localization pattern in the centriole lumen. Together, LRRCC1 and C2CD3 delineate a structure reminiscent of a filamentous density observed by electron microscopy in flagellates, termed the 'acorn'. Functionally, the depletion of LRRCC1 in human cells induced defects in centriole structure, ciliary assembly and ciliary signaling, supporting that LRRCC1 cooperates with C2CD3 to organizing the distal region of centrioles. Since a mutation in the *LRRCC1* gene has been identified in Joubert syndrome patients, this finding is relevant in the context of human ciliopathies. Taken together, our results demonstrate that rotational asymmetry is an ancient property of centrioles that is broadly conserved in human cells. Our work also reveals that asymmetrically localized proteins are key for primary ciliogenesis and ciliary signaling in human cells.

46 **Introduction**

47

48 Centrioles are cylindrical structures with a characteristic ninefold symmetry, which results
49 from the arrangement of their constituent microtubule triplets (LeGuennec et al., 2021). In
50 animal cells, centrioles are essential for the assembly of centrosomes and cilia. The centrosome,
51 composed of two centrioles embedded in a pericentriolar material (PCM), is a major organizer
52 of the microtubule cytoskeleton. In addition, most vertebrate cells possess a primary cilium, a
53 sensory organelle that assembles from the oldest centriole within the centrosome, called mother
54 centriole (Kumar and Reiter, 2021).

55 Centrioles within the centrosome show no apparent rotational asymmetry, *i.e.,* no
56 structural asymmetry of the microtubule triplets. In vertebrates, the mother centriole carries
57 distal appendages (DAs) and subdistal appendages arranged in a symmetric manner around the
58 centriole cylinder (Kumar and Reiter, 2021). In contrast, the centriole/basal body complex of
59 flagellates, to which the animal centrosome is evolutionary related, is characterized by marked
60 rotational asymmetries (Azimzadeh, 2021; Yubuki and Leander, 2013). In flagellates, an array
61 of fibers and microtubules anchored asymmetrically at centrioles controls the spatial
62 organization of the cell (Feldman et al., 2007; Yubuki and Leander, 2013). The asymmetric
63 attachment of cytoskeletal elements appears to rely on molecular differences between
64 microtubule triplets. In the green alga *Chlamydomonas reinhardtii,* Vfl1p (Variable Flagella
65 number 1 protein) localizes principally at two triplets near the attachment site of a striated fiber
66 connecting the centrioles (Silflow et al., 2001). This fiber is absent or mispositioned in the *vfl1*
67 mutant, leading to defects in centriole position and number, and overall cytoskeleton
68 disorganization (Adams et al., 1985; Feldman et al., 2007). In the same region, a rotationally
69 asymmetric structure termed the 'acorn' was observed in the centriole lumen by transmission

electron microscopy. The acorn appears as a filament connecting five successive triplets and is in part colocalized with Vfl1p (Geimer and Melkonian, 2005, 2004).

We recently established that Vfl1p function is conserved in the multiciliated cells (MCCs) of planarian flatworms, which was recently confirmed in xenopus (Basquin et al., 2019; Nommick et al., 2022). MCCs assemble large numbers of centrioles that are polarized in the plane of the plasma membrane to enable the directional beating of cilia (Meunier and Azimzadeh, 2016), like in *C. reinhardtii*. The planarian ortholog of Vfl1p is required for the assembly of two appendages that decorate MCC centrioles asymmetrically, the basal foot and the ciliary rootlet (Basquin et al., 2019). Depleting Vfl1p orthologs in planarian or xenopus MCCs alters centriole rotational polarity, reminiscent of the *vfl1* phenotype in *C. reinhardtii* (Adams et al., 1985; Basquin et al., 2019; Nommick et al., 2022). Intriguingly, the human ortholog of Vfl1p, called LRRCC1 (Leucine Rich Repeat and Coiled Coil containing 1) localizes at the centrosome despite the lack of rotationally asymmetric appendage in this organelle (Andersen et al., 2003; Muto et al., 2008). Furthermore, a homozygous mutation in the *LRRCC1* gene was identified in two siblings affected by a ciliopathy called Joubert syndrome (JBTS), suggesting that LRRCC1 might somehow affect the function of non-motile cilia (Shaheen et al., 2016).

Here, we show that LRRCC1 localizes in a rotationally asymmetric manner in the centrioles of the human centrosome. We further establish that LRRCC1 is required for proper ciliary assembly and signaling, which likely explains its implication in JBTS. LRRCC1 affects the recruitment at centrioles of another ciliopathy protein called C2CD3 (C2 domain containing 3), which we found to also localize in a rotationally asymmetric manner, forming a pattern partly reminiscent of the acorn described in flagellates. Our findings uncover the unanticipated

94 rotational asymmetry of centrioles in the human centrosome and show that this property is
95 connected to the assembly and function of primary cilia.
96

97 # Results

98

99 **LRRCC1 localizes asymmetrically at the distal end of centrioles**

100 To investigate a potential role of LRRCC1 at the centrosome, we first sought to determine its
101 precise localization. We raised antibodies against two different fragments within the long C-
102 terminal coiled-coil domain of LRRCC1 (Ab1, 2), which both stained the centrosome region
103 in human Retinal Pigmented Epithelial (RPE1) cells (Fig. 1a; Supplemental Fig. S1a), as
104 previously reported (Muto et al., 2008). Labeling intensity was decreased in LRRCC1-depleted
105 cells for both antibodies, supporting their specificity (Fig. 4a, b; Supplemental Fig. S1d, e, g).
106 LRRCC1 punctate labeling in the centrosomal region indicated that it is present within
107 centriolar satellites, confirming a previous finding that LRRCC1 interacts with the satellite
108 component PCM1 (Gupta et al., 2015). After nocodazole depolymerization of microtubules to
109 disperse satellites, a fraction of LRRCC1 was retained at centrioles (Fig. 1a; Supplemental Fig.
110 S1a), providing evidence that LRRCC1 is also a core component of centrioles. To determine
111 LRRCC1 localization more precisely within the centriolar structure, we used ultrastructure
112 expansion microscopy (U-ExM) (Gambarotto et al., 2019) combined with imaging on a Zeiss
113 Airyscan 2 confocal microscope, thereby increasing the resolution by a factor of ~ 8 compared
114 to conventional confocal microscopy. We found that LRRCC1 localizes at the distal end of
115 centrioles as well as of procentrioles (Fig. 1b). Strikingly, and unlike other known centrosome
116 components, LRRCC1 decorated the distal end of centrioles in a rotationally asymmetric
117 manner. Indeed, LRRCC1 was detected close to the triplet blades and towards the lumen of the
118 centriole (Fig. 1c). The staining was often associated with two or more consecutive triplets,
119 one of them being usually more brightly labelled than the others. In addition, a fainter staining
120 was consistently detected along the entire length of all triplets (Fig. 1b, brighter exposure). This
121 pattern was observed in both RPE1 and HEK 293 cells and was obtained with both anti-

122 LRRCC1 antibodies (Supplemental Fig. S1h), supporting its specificity. We verified that
123 LRRCC1 asymmetric localization was also observed in unexpanded cells by directly analyzing
124 immunofluorescence samples by Airyscan microscopy (Fig. 1d). We measured the lateral
125 distribution of LRRCC1 signal intensity peak relative to the long axis of the centriole. The
126 distance between peaks was greater for LRRCC1 than for hPOC5, a marker that localizes
127 symmetrically in the centriole (Azimzadeh et al., 2009; le Guennec et al., 2020), confirming
128 the asymmetry of LRRCC1 staining. The distal pattern obtained by U-ExM showed some
129 variability, especially in the distance between LRRCC1 and the centriole wall (Fig. 1c), which
130 could result from the fact that centrioles were not perfectly orthogonal to the imaging plan. To
131 obtain a more accurate picture of LRRCC1 localization, we generated 3D reconstructions that
132 we realigned, first along the vertical axis, then with respect to one another using the most
133 intense region of the LRRCC1 labeling as a reference point (Fig. 1e; Supplemental Fig. S2a-
134 b). An average 3D reconstruction was then generated (Fig. 1f) and revealed that LRRCC1 was
135 mainly associated to one triplet, and to a lesser extent to its direct neighbor counterclockwise,
136 on their luminal side. A longitudinal view confirmed that LRRCC1 is principally located at the
137 distal end of centrioles.

138 Together, our results show that LRRCC1 is localized asymmetrically within the distal
139 centriole lumen, establishing that centrioles within the human centrosome are rotationally
140 asymmetric.

141

142 **The localization pattern of LRRCC1 is similar at the centrosome and in mouse MCCs**

143 LRRCC1 orthologs are required for establishing centriole rotational polarity in planarian and
144 xenopus MCCs, like in *C. reinhardtii* (Basquin et al., 2019; Nommick et al., 2022; Silflow et
145 al., 2001). It is therefore plausible that LRRCC1-related proteins localize asymmetrically in
146 MCC centrioles, and indeed, Lrrcc1 was recently found associated to the ciliary rootlet in

147 xenopus MCCs (Nommick et al., 2022). To determine whether LRRCC1 also localizes at the
148 distal end of MCC centrioles in addition to its rootlet localization, and if so, whether LRRCC1
149 localization pattern resembles that observed at the centrosome, we analyzed mouse ependymal
150 and tracheal cells by U-ExM. In *in vitro* differentiated ependymal cells, the labeling generated
151 by the anti-LRRCC1 antibody was consistent with our observations in human culture cells.
152 Mouse Lrrcc1 localized asymmetrically at the distal end of centrioles, opposite to the side
153 where the basal foot is attached (Fig. 2a), as determined by co-staining with the basal foot
154 marker γ-tubulin (Clare et al., 2014). Lrrcc1 was also present at the distal end of procentrioles
155 forming via either the centriolar or acentriolar pathways (*i.e.,* around parent centrioles or
156 deuterosomes, respectively) (Fig. 2b). We also examined tracheal explants, in which centrioles
157 were docked and polarized at the apical membrane in higher proportions (Fig. 2c). We obtained
158 an average image of Lrrcc1 labeling from 35 individual centrioles aligned using the position
159 of the basal foot as a reference point. This revealed that Lrrcc1 is principally located in the
160 vicinity of 3 triplets opposite to the basal foot, to the right of basal foot main axis (triplet
161 number 9, 1 and 2 on the diagram in Fig. 2d). Lrrcc1 was located farther away from the triplet
162 wall than in centrioles of the centrosome, but this was likely an effect of a deformation of the
163 centrioles (Fig. 2c, d) caused by the incomplete expansion of the underlying cartilage layer in
164 tracheal explants. In agreement, Lrrcc1 was close to the triplets in ependymal cell monolayers,
165 which expand isometrically. Besides the distal centriole staining, we found no evidence that
166 Lrrcc1 is associated to the ciliary rootlet in mouse MCCs, unlike in xenopus. The Lrrcc1 pattern
167 in mouse MCCs was thus similar to the pattern observed at the human centrosome.
168 Together, these results show that LRRCC1 asymmetric localization is a conserved feature
169 of mammalian centrioles, presumably linked to the control of centriole rotational polarity and
170 ciliary beat direction in MCCs.
171

172 **Procentriole assembly site is partly correlated with centriole rotational polarity**

173 In *C. reinhardtii*, cytoskeleton organization and flagellar beat direction depend on the position
174 and orientation at which new centrioles arise during cell division. Reflecting the stereotypical
175 organization of centrioles and procentrioles in this species, Vfl1p is recruited early and at a
176 fixed position at the distal end of procentrioles (Fig.3a) (Geimer and Melkonian, 2004; Silflow
177 et al., 2001). We therefore wondered whether this mechanism might be to some extent
178 conserved at the centrosome, which could explain the persistence of centriole rotational
179 asymmetry despite the absence of asymmetric appendages or ciliary motility in most animal
180 cell types. We first analyzed the timing of LRRCC1 incorporation into procentrioles. LRRCC1
181 was already present at an early stage of centriole assembly, when the procentrioles stained with
182 acetylated tubulin and the cartwheel component SAS-6 were only about 100 nm in length (Fig.
183 3b). LRRCC1 was then detected during successive stages of procentriole elongation, always
184 localizing asymmetrically and distally (Fig. 3c), like in *C. reinhardtii*. We then examined
185 LRRCC1 localization in duplicating centrosomes by generating 3D-reconstructions of
186 diplosomes (*i.e.,* orthogonal centriole pairs) from RPE1 and HEK 293 cells processed by U-
187 ExM (Fig. 3d). We analyzed two parameters: the angle between LRRCC1 in the procentriole
188 and the long axis of the parent centriole used as reference (Fig. 3d, LRRCC1 localization in
189 procentrioles), and the angle between procentriole position and LRRCC1 in the parent centriole
190 (Fig. 3d, Procentriole position with respect to centriolar LRRCC1). We found that LRRCC1
191 localization in procentrioles was more often aligned with the long axis of the parent centriole
192 in RPE1 cells (Fig. 3d, top left panel, quadrants Q1 and Q3, respectively), but less so in HEK
193 293 cells (top right panel), in which the distribution was closer to a random distribution. Thus,
194 human procentrioles do not arise in a fixed orientation, although there appears to be a bias
195 toward alignment of LRRCC1 with the main axis of the parent centriole in RPE1 cells. Next,
196 we analyzed the position of procentrioles with respect to centriolar LRRCC1 (bottom panels).

197 Based on current models, procentriole assembly is expected to occur at a random position
198 around parent centrioles in animal cells (Takao et al., 2019). Identification of LRRCC1
199 provided the first opportunity to directly test this model. In diplosomes from both RPE1 and
200 HEK 293 cells, the position of procentrioles with respect to LRRCC1 location in the parent
201 centriole was variable, confirming that the position at which procentrioles assemble is not
202 strictly controlled in human cells. Interestingly, however, the procentrioles were not distributed
203 in a completely random fashion either. Procentrioles were found in quadrant Q2 (45-135
204 degrees clockwise from LRRCC1 centroid) on average 4 times less often than in the other
205 quadrants, both in RPE1 and HEK 293 cells, suggesting that rotational polarity of the parent
206 centriole somehow impacts procentriole assembly.

207 Overall, these results suggest that centriole rotational polarity influences centriole
208 duplication, limiting procentriole assembly within a particular region of centriole periphery.
209 Nevertheless, procentrioles are not formed at a strictly determined position, suggesting that the
210 mechanisms involving the LRRCC1 ortholog Vfl1p in centriole duplication in *C. reinhardtii*
211 are not or not completely conserved at the centrosome.

212

213 **LRRCC1 is required for primary cilium assembly and ciliary signaling**

214 A previous report identified a homozygous mutation in a splice acceptor site of the *LRRCC1*
215 gene in two siblings diagnosed with JBTS (Shaheen et al., 2016), but how disruption of
216 LRRCC1 expression affects ciliary assembly and signaling has never been investigated. To
217 address this, we generated RPE1 cell lines deficient in LRRCC1 using two different
218 CRISPR/Cas9 strategies and targeting two different regions of the *LRRCC1* locus. We could
219 not recover null clones despite repeated attempts in RPE1 - both wild type and p53$^{-/-}$ (Izquierdo
220 et al., 2014), HEK 293 and U2-OS cells, suggesting that a complete lack of LRRCC1 is possibly
221 deleterious. Nevertheless, we obtained partially depleted mutant clones, including three RPE1

222 clones targeted in either exons 8-9 (clone 1.1) or exons 11-12 (clones 1.2 and 1.9). Clone 1.1
223 carries deletions in both copies of the *LRRCC1* gene (Supplemental Fig. S3a). However, long
224 in-frame transcripts are expressed at reduced levels through alternative splicing (Supplemental
225 Fig. S1c, S3b). These transcripts are expected to generate mutant protein isoforms carrying
226 deletions in the beginning of the coiled-coil region (Supplemental Fig. S3). In contrast, only
227 wild-type transcripts were detected in clones 1.2 and 1.9, which were present at approximately
228 30% of wild-type levels, as determined by quantitative RT-PCR (Supplemental Fig. S1c). We
229 could not evaluate the overall decrease in LRRCC1 levels since the endogenous LRRCC1
230 protein was not detected by Western blot (Supplemental Fig. S1b). However, we confirmed the
231 decrease in centrosomal LRRCC1 levels by immunofluorescence using the two different anti-
232 LRRCC1 antibodies (Fig. 4a; Supplemental Fig. S1d-e). The down-regulation of LRRCC1 in
233 CRISPR clones was overall of the same order as that achieved by RNAi, although treatment of
234 CRISPR clones with the more efficient siRNA (si LRRCC1-1) could further reduce LRRCC1
235 levels (Fig. 4a). Using Airyscan microscopy, we showed that LRRCC1 amounts were
236 decreased not only at centriolar satellites, but also at the centrioles themselves in CRISPR
237 clones (Fig. 4b). Interestingly, the decrease in centriolar LRRCC1 was less for clone 1.1 than
238 for the other clones, suggesting that the mutant isoforms produced in this clone have different
239 dynamics than wild-type LRRCC1. Following induction of ciliogenesis, the proportion of
240 ciliated cells was decreased in all three mutant clones compared to control cells (Fig. 4c). We
241 were unable to obtain stable RPE1 cell lines expressing tagged versions of LRRCC1, and
242 transient overexpression of LRRCC1 in wild-type cells led to a decrease in the proportion of
243 ciliated cells, making phenotype rescue experiments difficult to interpret. However, we used
244 RNAi as an independent method to verify the specificity of ciliary defects observed in CRISPR
245 clones. The proportion of ciliated cells was decreased by RNAi to a similar extent than in
246 CRISPR clones (Fig. 4c; Supplemental Fig. S1f). RNAi treatment of CRISPR clones did not

247 lead to a greater decrease in ciliary frequency, suggesting that loss of LRRCC1 only partially
248 inhibits ciliogenesis (Fig. 4c). Sensory ciliopathies like JBTS result to a large extent from
249 defective Hedgehog signaling (Romani et al., 2013). We determined the effect of LRRCC1-
250 depletion on Hedgehog signaling by measuring the ciliary accumulation of the activator
251 SMOOTHENED (SMO) upon induction of the pathway (Rohatgi et al., 2007). Depletion of
252 LRRCC1 by either CRISPR editing or RNAi led to a drastic decrease in SMO accumulation at
253 the primary cilium following induction of the Hedgehog pathway by SMO-agonist (SAG) (Fig.
254 4d, e), and reduced expression of the target gene *PTCH1* (Supplemental Fig. S1i) (Goodrich et
255 al., 1996). Taken together, our results demonstrate that LRRCC1 is required for proper ciliary
256 assembly and signaling in human cells, further establishing its implication in JBTS.
257

258 **Depletion of LRRCC1 induces defects in centriole structure**

259 Mutations in distal centriole components can alter centriole length regulation or the assembly
260 of DAs, which both result in defective ciliogenesis (Reiter and Leroux, 2017; Sharma et al.,
261 2021). We used U-ExM to search for possible defects in centriole structure in LRRCC1-
262 depleted RPE1 cells. We measured centriole length in CRISPR clone 1.9, which has the lowest
263 levels of centriolar LRRCC1 (Fig. 4b), and in clone 1.1, which expresses mutant isoforms of
264 LRRCC1. Centrioles were co-stained with anti-acetylated tubulin and an antibody against the
265 DA component CEP164 to differentiate mother and daughter centrioles. We observed an
266 increase in centriole length in clone 1.9 (Fig. 5a) compared to control cells (483 ± 53 nm for
267 mother and 372 ± 55 nm for daughter centrioles in clone 1.9; 427 ± 56 nm for mother and 320
268 ± 46 nm for daughter centrioles in control cells; mean ± SD). Although on a limited sample
269 size, we also observed abnormally long centrioles by transmission electron microscopy in this
270 clone (494 ± 73 nm in clone 1.9, N = 9; 429 ± 52 nm in control cells, N = 3; mean ± SD) (Fig.
271 5c). The increase in centriole length was not due to mitotic delay as previously observed (Kong

272 et al., 2020), since the duration of mitosis in clone 1.9 was similar as in control cells
273 (Supplemental Fig. S1k). In addition, although centriole length was not modified in clone 1.1,
274 further reduction of LRRCC1 levels by RNAi resulted in a significant increase in centriole
275 length compared to control cells (Fig. 5b). Next, we analyzed DA organization by labeling
276 CEP164, which localizes to the outer part of DAs (Fig. 5d) (Yang et al., 2018). In RPE1 control
277 cells, 80 ± 14 % of mother centriole had 9 properly shaped DAs, but this proportion fell to 57
278 ± 16 % and 44 ± 17 % (mean ± SD) in clones 1.1 and 1.9, respectively (Fig. 5e). Mutant clones
279 exhibited an increased proportion of centrioles with one or more abnormally shaped DAs (29
280 ± 17 % and 42 ± 18 % in clones 1.1 and 1.9, respectively, compared to 11 ± 11 % in control
281 cells; mean ± SD). We obtained similar results in a HEK 293 CRISPR clone expressing half
282 the control levels of LRRCC1 (Fig. 5f; Supplemental Fig. S1g). LRRCC1-depletion did not
283 affect overall CEP164 levels at mother centrioles in the CRISPR clones (Supplemental Fig.
284 S4a, d), consistent with the relatively mild defect in DA morphology observed by U-ExM. We
285 also analyzed the distribution of CEP83, a DA component that localizes closer to the centriole
286 wall (Yang et al., 2018). The proportion of centrioles with abnormal CEP83 labeling was not
287 significantly different between control cells and CRISPR clones. However, this proportion
288 became significantly lower than in the control after treating CRISPR clones with RNAi (41 ±
289 18 % and 48 ± 4 % in clones 1.1 and 1.9 treated with RNAi, respectively, compared to 77 ± 9
290 % in control cells; mean ± SD; Fig. 5g, h). Beyond these anomalies in centriolar structure,
291 LRRCC1-depleted cells showed no defect in centriole number, supporting that centriole
292 assembly is not affected by LRRCC1 down-regulation (Supplemental Fig. S1j).
293 Together, these results show that down-regulation of LRRCC1 affects the formation of
294 centriole distal structures, leading to centriole over-elongation and abnormal DA morphology.
295
296

297 **LRRCC1 and C2CD3 delineate a rotationally asymmetric structure in human centrioles**
298 We next wanted to determine whether LRRCC1 cooperates with other distal centriole
299 components. Proteins shown to be recruited early at procentriole distal end include CEP290
300 (Kim et al., 2008), OFD1 (Singla et al., 2010) and C2CD3 (Thauvin-Robinet et al., 2014). Of
301 particular interest, OFD1 and C2CD3 are required for DA assembly and centriole length
302 control, and mutations in these proteins have been implicated in sensory ciliopathies (Singla et
303 al., 2010; Thauvin-Robinet et al., 2014; Tsai et al., 2019; Lei Wang et al., 2018). We first
304 determined whether depletion of LRRCC1 either by CRISPR editing or by RNAi led to
305 modifications in the recruitment of these proteins within centrioles. We found no major
306 differences in the centrosomal levels of OFD1 and CEP290 compared to control cells
307 (Supplemental Fig. S4b, c, e, f). In contrast, C2CD3 levels were moderately increased in cells
308 depleted from LRRCC1 either by CRISPR editing (clones 1.1 and 1.9) or by RNAi (Fig. 6a,
309 b). We thus analyzed C2CD3 further by U-ExM. As described previously, C2CD3 localized
310 principally at the distal extremity of centrioles (Fig. 6c) (Tsai et al., 2019; Yang et al., 2018).
311 Strikingly, the C2CD3 labeling was also asymmetric, often adopting a C-shape (Fig. 6d). After
312 correcting the vertical alignment of centrioles as previously, we generated an average 3D
313 reconstruction of the C2CD3 pattern. To do this, we used one end of the C as a reference point
314 in the xy-plane to superimpose individual centriole views. The resulting image supported that
315 the C2CD3 labeling forms a C-shaped pattern positioned symmetrically in the centriole lumen
316 (Fig. 6e). To determine whether the C2CD3 localization pattern is affected by LRRCC1-
317 depletion, we next analyzed C2CD3 in LRRCC1 CRISPR clones 1.1 and 1.9. The C2CD3
318 pattern was more variable than in control RPE1 cells, and often appeared abnormal in shape,
319 position, or both (Fig. 6f). Indeed, averaging the signal from multiple LRRCC1-depleted
320 centrioles produced aberrant patterns, most strikingly for clone 1.9 (clone 1.9; Fig. 6g).
321 Furthermore, the phenotype of clone 1.1 was enhanced by further reducing LRRCC1 levels

322 using RNAi (Fig. 6g). Thus, LRRCC1 is required for the proper assembly of the C2CD3-
323 containing distal structure.

324 To determine whether LRRCC1 and C2CD3 might belong to a common structure, we next
325 examined their respective positions within the centriole. We co-stained centrioles with our anti-
326 LRRCC1 antibody and a second anti-C2CD3 antibody produced in sheep (Table 1). We
327 confirmed that LRRCC1 and C2CD3 are present in the same distal region of the centriole (Fig.
328 7a). In transverse views, the two proteins were usually not perfectly colocalized but found in
329 close vicinity of one another near the microtubule wall. However, C2CD3 distal staining was
330 consistently fainter than with the previous antibody, and we either could not observe a full C-
331 shaped pattern, or we could not image it due to fluorescence bleaching. Neither anti-C2CD3
332 antibodies worked in mouse, so we were not able to compare C2cd3 and Lrrcc1 localization in
333 MCCs. Nevertheless, the results obtained by individually labeling LRRCC1 and C2CD3 at the
334 centrosome (Fig. 1f, 6e) together with the co-localization data (Fig. 7a) are consistent with the
335 hypothesis that LRRCC1 is located along the C2CD3-containing, C-shaped structure (Fig. 7b).
336 C2CD3 was not co-immunoprecipitated with a GFP-LRRCC1 fusion protein however,
337 suggesting that LRRCC1 and C2CD3 do not directly interact (Supplemental Fig. S5).

338 Taken together, our results support that C2CD3 localizes asymmetrically in the distal
339 lumen of human centrioles, a pattern that depends in part on LRRCC1.

340

341

342 **Discussion**

343

344 Here, we show that centrioles within the human centrosome are rotationally asymmetric despite
345 the apparent nine-fold symmetry of their ultrastructure. This asymmetry is manifested by a
346 specific enrichment in LRRCC1 near two consecutive triplets, and the C-shaped pattern of
347 C2CD3. Depletion of LRRCC1 perturbed the recruitment of C2CD3 and induced defects in
348 centriole structure, ciliogenesis and ciliary signaling, supporting that LRRCC1 contributes to
349 organizing the distal centriole region together with C2CD3. LRRCC1 localizes like its *C.*
350 *reinhardtii* ortholog Vfl1p*,* and C2CD3 delineates a filamentous structure reminiscent of the
351 acorn first described in *C. reinhardtii* (Geimer and Melkonian, 2005, 2004) and later found in
352 a wide variety of eukaryotic species (Cavalier-Smith, 2021; Vaughan and Gull, 2016).
353 Collectively, our results support that rotational asymmetry is a conserved property of centrioles
354 linked to ciliary assembly and signaling in humans.

355

356 **LRRCC1 and C2CD3 belong to a conserved rotationally asymmetric structure**

357 Our work identifies two proteins located asymmetrically in the distal centriole lumen of the
358 human centrosome, each with a specific pattern. LRRCC1 localizes principally near two
359 consecutive triplets, with the first triplet counterclockwise labelled approximately 50 % more
360 than the next one. This pattern is highly reminiscent of the LRRCC1 ortholog Vfl1p, which
361 localizes predominantly to the triplet facing the second centriole (referred to as triplet 1), and
362 to a lesser extent to its immediate neighbor counterclockwise (triplet 2; Fig. 7b) (Silflow et al.,
363 2001). In *C. reinhardtii*, triplets 1 and 2 are positioned directly opposite to the direction of
364 flagellar beat, which is directed towards triplet 6 (Fig. 7b) (Lin et al., 2012). In mouse MCCs,
365 Lrrcc1 is associated to triplets located not exactly opposite to the basal foot but with a clockwise
366 shift of at least 20° from the basal foot axis. However, the beating direction was shown to be

367 also shifted approximately 20° clockwise relative to the position of the basal foot in bovine
368 tracheal MCCs (Schneiter et al., 2021) (Fig. 2d). The position of Lrrcc1/Vfl1p-labelled triplets
369 with respect to ciliary beat direction might thus be similar in *C. reinhardtii* and in animal
370 MCCs. Overall, the specific localization pattern of Vfl1p-related proteins at the distal end of
371 centrioles, and their requirement for centriole positioning and ciliary beat orientation when
372 motile cilia are present, appear to be conserved between flagellates and animals.

373 The second protein conferring rotational asymmetry to human centrioles, C2CD3, delineates
374 a C-shape in the distal lumen. Strikingly, this staining is reminiscent of a filament observed by
375 electron microscopy, which is said to form an 'incomplete circle' in the distal lumen of human
376 centrioles (Vorobjev and Chentsov, 1980). Several lines of evidence favor the hypothesis that
377 the C2CD3-containing structure is homologous to the acorn, a conserved filamentous structure
378 that in *C. reinhardtii* connects five consecutive triplets along the centriole wall and across the
379 lumen (Fig. 7b) (Cavalier-Smith, 2021; Geimer and Melkonian, 2004; Vaughan and Gull,
380 2016). First, the C2CD3 labeling is consistent with a circular filament. Second, C2CD3 is
381 partially co-localized with LRRCC1 near the microtubule wall. And last, C2CD3 orthologs are
382 found in a variety of flagellated unicellular eukaryotes, including the green algae *Micromonas*
383 *pusilla* (Zhang and Aravind, 2012) and *Chlamydomonas eustigma* (Uniprot_A0A250XH15),
384 suggesting an ancestral association to centrioles and cilia. The partial co-localization of Vfl1p
385 and the acorn in *C. reinhardtii*, and the observation that both are already present at the distal
386 end of procentrioles, led to propose that Vfl1p might also be a component of the acorn (Geimer
387 and Melkonian, 2004). Consistent with this idea, both LRRCC1 and C2CD3 are recruited early
388 to the distal end of human procentrioles, and LRRCC1 is required for proper assembly of the
389 C2CD3-containing structure. C2CD3 recruitment at the centrioles also depends on the proteins
390 CEP120 and Talpid3 (Tsai et al., 2019). Future work will help deciphering the relationships

391 between these different proteins and characterize in more details the architecture of the
392 rotationally asymmetric structure at the distal end of mammalian centrioles.
393
394 **Rotationally asymmetric centriole components are required for ciliogenesis**
395 Our results uncover a link between centriole rotational asymmetry and primary ciliogenesis in
396 human cells. Mutations in C2CD3 have been involved in several sensory ciliopathies, including
397 JBTS (Boczek et al., 2018; Cortés et al., 2016; Ooi, 2015; Thauvin-Robinet et al., 2014). The
398 associated ciliary defects are likely caused by anomalies in the structure of centrioles, since
399 depleting C2CD3 inhibits centriole elongation and DA assembly, whereas C2CD3
400 overexpression leads to centriole hyper-elongation (Thauvin-Robinet et al., 2014; Wang et al.,
401 2018; Ye et al., 2014). We observed similar defects in LRRCC1-depleted cells, but of
402 comparatively lesser extent. DA morphology was altered, and centriole length was slightly
403 increased in cells depleted from LRRCC1. The fact that LRRCC1-depletion has a more limited
404 impact on centriole assembly than perturbation of C2CD3 levels suggests that LRRCC1 might
405 not be directly involved in centriole length control or DA formation, however. The defects
406 observed in LRRCC1-depleted cells could instead result indirectly from the abnormal
407 localization of C2CD3. Besides the defects in centriole structure, it is plausible that LRRCC1-
408 depletion also perturbs the organization of the ciliary gate, as LRRCC1-depleted cells exhibited
409 a drastic reduction in Hedgehog signaling. Loss of ciliary gate integrity interferes with the
410 accumulation of SMO in the cilium upon activation of the Hedgehog pathway and is a frequent
411 consequence of ciliopathic mutations (Garcia-Gonzalo and Reiter, 2017). The ciliary gate
412 consists of the TZ and the DA region, which both contribute to regulating protein trafficking
413 in and out of the cilium (Garcia-Gonzalo and Reiter, 2017; Nachury, 2018). The anomalies in
414 DA morphology observed in LRRCC1-depleted cells could disrupt the organization of the so-
415 called DA matrix (Yang et al., 2018), thus preventing SMO accumulation in the cilium.

416 Another, non-mutually exclusive possibility is that the architecture of the TZ, which forms
417 directly in contact with the distal end of the centriole, is altered by LRRCC1-depletion. In either
418 case, our observations in RPE1 cells are consistent with the JBTS diagnosis in two siblings
419 carrying a mutation in the *LRRCC1* gene (Shaheen et al., 2016), further establishing that
420 *LRRCC1* is a novel ciliopathy gene. Besides signaling, ciliary gate integrity is required for
421 axoneme extension and indeed, LRRCC1-depleted cells formed cilia at lower frequency than
422 control cells – a defect that might also result from perturbed DA architecture. In the *vfl1* mutant
423 of *C. reinhardtii*, both unanchored centrioles, and centriole docked at the plasma membrane
424 but lacking a flagellum were observed (Adams et al., 1985). This supports that LRRCC1/Vfl1p
425 requirement for properly assembling the ciliary gate is a conserved functional aspect of this
426 family of proteins (Fig. 7c).

427 Why is there a rotationally asymmetric structure at the base of primary cilia, and how does
428 this structure form and contribute to the assembly of the DAs and the cilium remain open
429 questions. In *C. reinhardtii* and in MCCs, LRRCC1 function is linked to the assembly of
430 asymmetric appendages, which must be correctly positioned in relation to ciliary beat direction
431 (Fig. 7c). An asymmetric structure present early during centriole assembly and ultimately
432 located near the cilium appears well suited for this task. The conservation of such a structure
433 at the base of the primary cilium could perhaps indicate that primary cilia also possess
434 rotationally asymmetric features, which would open interesting new perspectives on ciliary
435 roles in heath and disease.

436

437 **Other roles for centriole rotational asymmetry in human cells**

438 Our finding that procentrioles do not form completely at random with respect to LRRCC1
439 location in the parent centriole suggests that centriole rotational polarity can influence centriole
440 duplication in human cells. In *C. reinhartdtii*, procentrioles are formed at fixed positions with

respect to the parent centrioles, to which they are bound by a complex array of fibrous and microtubular roots (Fig. 7c) (Geimer and Melkonian, 2004; Yubuki and Leander, 2013). The process is likely different at the centrosome since the roots typical of flagellates are not conserved in animal cells (Azimzadeh, 2021; Yubuki and Leander, 2013). In mammalian cells, procentrioles form near the wall of the parent centriole following the recruitment of early centriole proteins directly to the PCM components CEP152 and CEP192 (Yamamoto and Kitagawa, 2021). It is nonetheless conceivable that an asymmetry in triplet composition could result in local changes in PCM composition, which in turn could negatively impact PLK4 activation in this region. For instance, our analyses in planarian MCCs led us to postulate that linkers might be tethered to one side of the centrioles in a VFL1-dependent manner and independently of centriole appendages (Basquin et al., 2019). Future work will allow deciphering how centriole rotational asymmetry influences centriole duplication, and whether it affects other aspects of centriole positioning and cellular organization.

Acknowledgements

The authors are deeply grateful to Marine Laporte, Virginie Hamel, Paul Guichard and Davide Gambarotto for teaching them the U-ExM procedure and for sharing antibodies; Arnaud Echard and Takashi Ochi for critical reading of the manuscript; Amélie-Rose Boudjema and Alice Meunier for providing mouse ependymal cells and Isabelle Le Parco for the tracheal tissue; Juliane Da Graça and Simon Herman for technical help; Rémi Le Borgne for help with transmission electron microscopy and for critical reading of the manuscript. We acknowledge the core imaging facility of Institut Jacques Monod (ImagoSeine facility, member of the France BioImaging infrastructure supported by grant ANR-10-INBS-04 from the French National Research Agency). This work was supported by funding from La Ligue Contre le Cancer, Fondation ARC pour la recherche sur le cancer and ANR-21-CE13-008 to J.A. N.G. was

466 recipient of a MESRI PhD fellowship from the French Government and a 4th year PhD
467 fellowship from the Fondation pour la Recherche Médicale.

468

469 **Declaration of interests**

470 The authors declare no competing interests.

471

472 # Material and Methods

473

474 **Cell culture**

475 RPE1 cells (hTERT-RPE1, RRID:CVCL_4388) were cultured in DMEM/F-12 medium
476 (ThermoFisher Scientific) supplemented with 10 % fetal calf serum (ThermoFisher Scientific),
477 100 U/mL penicillin and 100 µg/mL streptomycin (ThermoFisher Scientific). Ciliogenesis was
478 induced by culturing RPE1 cells in medium without serum during 48 hours. HEK 293 cells
479 (kind gift from F. Causeret, Institut Imagine, Paris) were cultured in DMEM medium
480 (ThermoFisher Scientific) supplemented with 10 % fetal calf serum and antibiotics as
481 previously. All cells were kept at 37°C in the presence of 5 % CO_2.

482

483 **Mouse ependymal cells and tracheal tissue**

484 All experiments were performed in accordance with French Agricultural Ministry and
485 European guidelines for the care and use of laboratory animals. *In vitro* differentiated
486 ependymal cells were a kind gift from A.R. Boudjema and A. Meunier (IBENS, Paris). They
487 were prepared as described previously (Delgehyr et al., 2015; Mercey et al., 2019) from
488 Cen2GFP mice (CB6-Tg(CAG-EGFP/CETN2)3-4Jgg/J, The Jackson Laboratory). The
489 fragment of trachea was obtained from a wild-type mouse of the Swiss background (kindly
490 provided by I. Le Parco, Institut Jacques Monod).

491

492 **CRISPR/Cas9 editing**

493 LRRCC1 mutant clones were obtained by two different CRISPR/Cas9 strategies. First, RPE1
494 cells were co-transfected with plasmid px154-1 (U6p-gRNA#1_U6p-gRNA#2_CMVpnCas9-
495 EGFP_SV40p-PuroR-pA with gRNA#1: 5'- AGA ATT CTA CCC TAC CTG - 3' and
496 gRNA#2: 5'- TAA GGT AGT GCT TCC TAC -3') targeting the *LRRCC1* locus in exon 8, and

497 px155-24 (U6p-gRNA#3_U6p-gRNA#4_CMVpnCas9-mCherry_SV40p-PuroR-pA;
498 gRNA#1: 5'- ATC TAC TCG GAA AGC TGA -3' and 5'- GCT TGA GGG CTC AAA TAC
499 - 3') targeting exon 9. Both constructs express the nickase mutant of Cas9 fused to either EGFP
500 or mCherry. Two days after transfection, EGFP- and mCherry-positive cells were sorted by
501 flow cytometry and grown at low concentration. Individual clones were picked after 2 weeks
502 and analyzed by PCR to detect short insertions/deletions. A single clone was obtained (clone
503 1.1), which was further characterized by genomic sequencing. Both alleles of *LRRCC1*
504 contained deletions (~ 0.6 kb deletion of exon 9 and a ~1.5 kb deletion of exon 8; Supplemental
505 Fig. S3a) leading to frameshifts. In a second approach, cells were co-transfected using a mix
506 of 3 CRISPR/Cas9 Knockout Plasmids (sc-413781; Santa Cruz Biotechnology) targeting exons
507 11 (5'- CTT GTT CTC TTT CTC GAT GA– 3' and 5' - ACT TCT TGC ATT GAA AGA AC
508 - 3') or 12 (5' - CGT GTT AAG CCA GCA GTA TA– 3') of *LRRCC1,* together with the
509 corresponding Homology Directed Repair plasmids carrying a puromycine-resistance cassette
510 (sc-413781-HDR; Santa Cruz Biotechnology), following the recommendations of the
511 manufacturer. Mutant clones were selected by addition of 2 µg/mL puromycine in the culture
512 medium and further screened by immunofluorescence, allowing to identify two clones with
513 decreased LRRCC1 levels (clones 1.2 and 1.9). Genomic insertion of the HDR cassette could
514 not be detected in these clones by PCR, and no sequence anomalies were identified in PCR
515 fragments corresponding to exons 10 to 13. This suggests that one copy of the *LRRCC1* gene
516 is intact, while the second copy may have undergone more extensive modifications via large
517 deletions/insertions. For sequencing of LRRCC1 transcripts, total RNA extracts were obtained
518 using the Nucleospin RNA kit (Macherey-Nagel) and cDNAs were synthesized using
519 SuperScript III reverse transcriptase (Thermofisher Scientific). PCR primers specific to exons
520 4 and 8, 4 and 9, 8 and 19, or 9 and 19 were used to amplify cDNAs from clone 1.1; primers

521 specific to exons 4 and 17 were used for clones 1.2 and 1.9. The resulting fragments were
522 analyzed by sequencing.
523
524 **Inducible HEK 293 cell lines**
525 LRRCC1 full-length coding sequence was amplified from cDNA clone IMAGE:5272572
526 (Genbank accession: BC070092.1), corresponding to the longest isoform of LRRCC1
527 (NM_033402.5), after correction of a frameshift error by PCR mutagenesis. As N- and C-
528 terminal GFP fusions were not targeted to the centrosome, we inserted the GFP tag within the
529 LRRCC1 sequence in disordered regions present between the leucine rich repeat and coiled-
530 coil domains, either after amino acid 251 or 402. The fusions were cloned into the pCDNA-
531 5FRT (ThermoFischer Scientific) vector using the Gibson assembly method (Gibson et al.,
532 2009) and then integrated into the Flp-In-293 cell line using the Flp-In system (ThermoFischer
533 Scientific). Expression of the GFP-LRRCC1 fusions was induced by culturing the Flp-In-293
534 cell lines overnight in medium supplemented with 1 µg/mL doxycycline (ThermoFischer
535 Scientific).
536
537 **RNAi**
538 Ready to use double-stranded siRNA LRRCC1-si1 (target sequence: 5'- AAG GAG AAA
539 GAT GGA GAC GAT - 3') (Muto et al., 2008), LRRCC1-si2 (target sequence: 5'- TTA GAT
540 GAC CAA ATT CTA CAA - 3') and control siRNA (AllStars Negative Control) were
541 purchased from Qiagen. siRNAs were delivered into cells using Lipofectamine RNAiMAX
542 diluted in OptiMEM medium (ThermoFisher Scientific). Cells were fixed after 48 hours and
543 processed for immunofluorescence. For RNAi-depletion of ciliated cells, RPE1 cells grown in
544 complete culture medium were treated by RNAi, incubated for 2 days, then submitted to a

545 second round of RNAi. After 8 hours, cells were washed 3 x in PBS then cultured during 24
546 hours in serum-free medium to induce ciliogenesis.
547
548 **qRT-PCR**
549 Total RNA extracts were obtained using the Nucleospin RNA kit (Macherey-Nagel) and
550 cDNAs were synthetized using SuperScript III reverse transcriptase (Thermofisher Scientific).
551 qPCR was performed in triplicate with the GoTaq qPCR Master Mix (Promega) in a
552 LightCycler 480 instrument (Roche) using the primers listed in Table 2. Quantification of
553 relative mRNA levels was performed using CHMP2A and EMC7 as reference genes following
554 the MIQE guidelines (Bustin et al., 2009).
555
556 **Antibodies**
557 Fragments encoding either aa 671-805 (Ab1) or aa 961-1032 (Ab2) of LRRCC1
558 (NP_208325.3) were cloned in pGST-Parallel1 and expressed in *Escherichia coli.* The GST-
559 fusion proteins were purified under native conditions using glutathione agarose (ThermoFisher
560 Scientific) and the LRRCC1 fragments were recovered by Tev protease cleavage and dialyzed
561 before rabbit immunization (Covalab). Antibodies were affinity-purified over the
562 corresponding GST-LRRCC1 fusion bound to Affi-Gel 10 resin (Bio-Rad). Other primary and
563 secondary antibodies used in this study are listed in Table 1.
564
565 **Western blot**
566 For whole-cell extracts, Flp-In-293 cell lines expressing the GFP-LRRCC1 fusions were
567 induced overnight with doxycycline, collected by centrifugation, and resuspended in Western
568 blot sample buffer prior to incubation at 95 °C for 5 minutes. For immunoprecipitation
569 experiments, doxycycline-induced cells expressing LRRCC1 with a GFP inserted after aa 402

570 were resuspended in lysis buffer (50 mM Tris pH 8, 150 mM NaCl, 1 % NP-40, 0.5 % sodium
571 deoxycholate, 0.1 % SDS) supplemented with 1 mM $MgCl_2$, 20 µg/mL DNAse I (Roche) and
572 a protease inhibitor cocktail (Complete mini, EDTA-free, Roche). After 30 minutes on ice, the
573 lysates were centrifuged at 15 000 g for 10 minutes at 4°C. The supernatants were then
574 incubated with Dynabeads M-280 sheep-anti rabbit magnetic beads (ThermoFischer Scientific)
575 previously incubated with rabbit anti-IgGs, either anti-GFP or anti-HA tag for the control IP
576 (Table 1), and rotated for 3 hours at 4°C. After 3 washes with lysis buffer, immunoprecipitated
577 proteins were recovered by resuspending the beads in sample buffer and heating at 95 °C for 5
578 minutes. The samples were then run on 4-20% Mini-Protean TGX precast protein gels (Bio-
579 Rad) and transferred onto PVDF membrane using the iBlot 2 blot system (ThermoFischer
580 Scientific). The membranes were blocked and incubated with antibodies following standard
581 procedures, then visualized using Pierce ECL plus chemiluminescence reagents
582 (ThermoFischer Scientific) on a ChemiDoc imaging system (Bio-Rad).
583
584 **Immunofluorescence**
585 Cells were fixed in cold methanol for 5 minutes at – 20 °C, blocked 10 minutes with 3 % BSA
586 (Sigma Aldrich) in PBS containing 0.05 % Tween-20 (PBST-0.05%), then incubated with
587 primary antibodies diluted in PBST-0.05% containing 3 % BSA for 1 hour. After washing 3 x
588 1 minute in PBST-0.05%, cells were incubated 2 hours with secondary antibodies in PBST-
589 0.05% containing 3 % BSA and 5 µg/mL Hoechst 33342 (ThermoFischer Scientific), washed
590 in PBST-0.05% as previously, and mounted using Fluorescence Mounting Medium (Agilent).
591 For staining of primary cilia with anti-acetylated tubulin, cells were incubated 2 hours on ice
592 prior to methanol fixation. For quantification of SMO accumulation within cilia, confluent cells
593 cultured during 24 hours in serum-free medium were supplemented with 200 nM SAG (Sigma)
594 diluted in DMSO, or DMSO alone for 24 hours. Cells were then co-stained for SMO and

595 ARL13B to determine the position of the primary cilium. For all experiments involving
596 induction of ciliogenesis by serum deprivation, we verified that cells were arrested in G0 by
597 immunofluorescence staining of Ki67. To visualize centriolar LRRCC1, and to quantify
598 CEP290 centrosomal levels, cells were treated during 1 hour with 5 µM nocodazole prior to
599 fixation. Images were acquired using an Axio Observer Z.1 microscope (Zeiss) equipped with
600 a sCMOS Orca Flash4 LT camera (Hamamatsu) and a 63x objective (Plan Apo, N.A. 1.4). The
601 structured illumination microscopy (SIM) image was acquired on an ELYRA PS.1 (Zeiss)
602 equipped with an EMCCD iXon 885 camera (Andor) and a 63x objective (Plan Apo, N.A. 1.4).
603

604 **Ultrastructure expansion microscopy**

605 We used the U-ExM protocol described in (Gambarotto et al., 2019) with slight modifications.
606 Cells grown on glass coverslips were incubated in a fresh solution of 1 % acrylamide and 0.7
607 % formaldehyde diluted in PBS. After incubating 5 hours to overnight at 37 °C, the coverslips
608 were washed with PBS and placed cells down on a drop of 35 µL monomer solution (19.3 %
609 sodium acrylate, 10 % acrylamide, 0.1 % bis-acrylamide in PBS) to which 0.5 % TEMED and
610 0.1 % ammonium persulfate were added just before use. The coverslips were incubated 5
611 minutes on ice then 1 hour at 37°C, then transferred to denaturation buffer (200 mM SDS, 200
612 mM NaCl, 50 mM Tris pH9) for 15 minutes with agitation to detach the gels from the
613 coverslips. The gels were then incubated in denaturation buffer 1.5 hours at 95 °C, washed 2 x
614 30 minutes in deionized water then incubated overnight in water at room temperature to allow
615 expansion of the gel. The gels were measured at this step to determine the coefficient of
616 expansion. After 2 x 10 minutes in PBS, the gels were cut into smaller pieces then incubated 3
617 hours at 37 °C with primary antibodies diluted in saturation buffer (3 % BSA, 0.05 % Tween-
618 20 in PBS). The gel fragments were then washed 3 x 10 minutes in PBST-0.1%, incubated 3 h
619 with secondary antibodies and washed in PBST-0.1% as previously. Finally, the gels were

620 incubated 2 x 30 minutes in de-ionized water then left to expand overnight in de-ionized water
621 to regain their maximum size. For U-ExM of mouse tracheal cells, a fragment of WT mouse
622 trachea (kind gift from I. Le Parco, IJM, Paris) was adhered on a poly-lysine coated coverslip
623 then processed as described above with the following modifications: for the first step, the
624 fragment of trachea was incubated overnight to 48 hours in 1 % acrylamide and 0.7 %
625 formaldehyde in PBS; they were placed 15 min on ice prior to the 1-hour incubation at 37 °C
626 and the transfer to denaturation buffer. Note that GFP fluorescence was quenched during U-
627 ExM processing, so the GFP-Cen2 construct expressed in ependymal cells was not detectable
628 in final samples. Gels were imaged on Lab-Tek chamber slides (0.15 mm) coated with poly-
629 lysine (ThermoFisher Scientific). Images were acquired at room temperature using either a
630 LSM780 confocal microscope (Zeiss) equipped with an oil 63x objective (Plan Apo, N.A. 1.4),
631 or an LSM980 confocal microscope with Airyscan 2 (Zeiss) equipped with an oil 63x objective
632 (Plan Apo, N.A. 1.4).
633
634 **Image analysis**
635 Protein levels were determined using ImageJ software (Schneider et al., 2012) by measuring
636 the fluorescence intensity in the centrosome or cilium area and subtracting the cytoplasmic
637 background in z-series taken at 0.5-µm interval. Images of individual centrioles in U-ExM are
638 maximum intensity projections of all z-sections comprising the signal of interest. Note that
639 centrioles are presented as they are in the sample (*i.e.,* without correcting their orientation),
640 which leads to an apparent shift between channels or decreased circularity in the projections
641 when centrioles are not parallel to the imaging axis. Analysis of distal appendage morphology
642 defects was performed on z-stacks and not on projected images. Daughter centriole length was
643 determined by U-ExM using the acetylated tubulin staining. For mother centrioles, which could
644 be associated with a primary cilium, the length was measured between the proximal end of the

645 acetylated tubulin staining and distal appendages labeled by anti-CEP164 or CEP83. To
646 generate average images of LRRCC1 and C2CD3, only centrioles that were nearly
647 perpendicular to the imaging plane were acquired on the Airyscan microscope in order to
648 maximize the resolution in transverse views. Calculating the average image consisted of several
649 steps: cropping out individual centrioles, aligning them, providing reference points,
650 standardizing centrioles using the reference points, and averaging (Supplemental Fig. S2). The
651 cropping was done in ImageJ, and for aligning and providing the reference points a graphical
652 user interface was developed based on Napari (Sofroniew et al., 2020). Centriole alignment:
653 the direction of centriole long axis was selected manually and used to position the centriole
654 vertically. Providing the reference points: reference points were manually selected to outline
655 the circle of microtubules triplets and the location of the protein of interest. The centriole was
656 also framed in Z dimension with a rectangle. Standardization: the reference points were used
657 to calculate all necessary transformations (rotation, scaling and translation) to map the original
658 image of a centriole to the standard image. Averaging: an average image was calculated for all
659 the successive XY planes of the standardized image stacks. For alignment of tracheal cell
660 centrioles, since the current version of the graphical user interface can only accommodate two
661 channels, the position of the basal foot provided by the γ-tubulin channel was reported
662 manually in the acetylated tubulin channel using Image J. The images were then processed as
663 before using the manual annotation as a reference point for the basal foot.
664 For analysis of procentriole position and LRRCC1 location in procentrioles, 3D-
665 reconstructions of diplosomes processed for U-ExM were obtained using IMARIS software
666 (Oxford Instruments).
667
668 **Electron microscopy**

669 RPE1 cells were grown at confluence before induction of ciliogenesis for 72 hours by serum
670 deprivation. Cells were fixed 30 minutes in 2.5 % glutaraldehyde (Electron Microscopy
671 Sciences), 2 % paraformaldehyde (Electron Microscopy Sciences), 1 mM $CaCl_2$ in PBS, then
672 washed 3 x 5 minutes in PBS. Samples were then post-fixed during 30 minutes in 1 % Osmium
673 tetroxide (Electron Microscopy Sciences), then washed 3 x 5 minutes in water. Dehydration
674 was performed using graded series of ethanol in water for 5 minutes 30%, 50%, 70%, 90%,
675 100%, 100%. Resin infiltration was performed by incubating 30 minutes in an Agar low
676 viscosity resin (Agar Scientific Ltd) and EtOH (1:2) mix, then 30 minutes in a resin and EtOH
677 (2:1) mix followed by overnight incubation in pure resin. The resin was then changed and the
678 samples further incubated during 1.5 hours prior to inclusion in gelatin capsules and overnight
679 polymerization at 60 °C. 70 nm sections were obtained using an EM UC6 ultramicrotome
680 (Leica), post-stained in 4 % aqueous uranyl acetate and lead citrate, and observed at 80 kV
681 with a Tecnai12 transmission electron microscope (ThermoFischer Scientific) equipped with a
682 1K×1K Keen View camera (OSIS).
683
684 **Videomicroscopy**
685 To determine the duration of mitosis, individual frames of cells growing under normal culture
686 conditions were acquired every 5 minutes for 24 hours using an IncuCyte ZOOM live-cell
687 analysis system (Sartorius) equipped with a 20 x objective.
688
689 **Statistical analysis**
690 All statistical analyses were performed using the Prism 9 for Mac OS X software (GraphPad
691 Software, Inc.). All values are provided as mean ± SD. The number of experimental replicates
692 and the statistical test used are indicated in the figure legends, and the p values are included
693 when statistically different.

694 **References**

695

696 Adams GM, Wright RL, Jarvik JW. 1985. Defective temporal and spatial control of flagellar
697 assembly in a mutant of Chlamydomonas reinhardtii with variable flagellar number. *J Cell*
698 *Biol* **100**:955–964.
699 Andersen JS, Wilkinson CJ, Mayor T, Mortensen P, Nigg EA, Mann M. 2003. Proteomic
700 characterization of the human centrosome by protein correlation profiling. *Nature*
701 **426**:570–574.
702 Azimzadeh J. 2021. Evolution of the centrosome, from the periphery to the center. *Current*
703 *Opinion in Structural Biology* **66**:96–103. doi:10.1016/j.sbi.2020.10.020
704 Azimzadeh J, Hergert P, Delouvée A, Euteneuer U, Formstecher E, Khodjakov A, Bornens M.
705 2009. hPOC5 is a centrin-binding protein required for assembly of full-length centrioles.
706 *Journal of Cell Biology* **185**. doi:10.1083/jcb.200808082
707 Basquin C, Ershov D, Gaudin N, Vu HT, Louis B, Papon JF, Orfila AM, Mansour S, Rink JC,
708 Azimzadeh J. 2019. Emergence of a Bilaterally Symmetric Pattern from Chiral
709 Components in the Planarian Epidermis. *Dev Cell* **51**:516-525 e5.
710 doi:10.1016/j.devcel.2019.10.021
711 Boczek NJ, Hopp K, Benoit L, Kraft D, Cousin MA, Blackburn PR, Madsen CD, Oliver GR,
712 Nair AA, Na J, Bianchi DW, Beek G, Harris PC, Pichurin P, Klee EW. 2018.
713 Characterization of three ciliopathy pedigrees expands the phenotype associated with
714 biallelic C2CD3 variants. *European Journal of Human Genetics* **26**:1797–1809.
715 doi:10.1038/s41431-018-0222-3
716 Bustin SA, Benes V, Garson JA, Hellemans J, Huggett J, Kubista M, Mueller R, Nolan T,
717 Pfaffl MW, Shipley GL, Vandesompele J, Wittwer CT. 2009. The MIQE guidelines:

718 minimum information for publication of quantitative real-time PCR experiments. *Clin*
719 *Chem* **55**:611–622. doi:10.1373/clinchem.2008.112797
720 Cavalier-Smith T. 2021. Ciliary transition zone evolution and the root of the eukaryote tree:
721 implications for opisthokont origin and classification of kingdoms Protozoa, Plantae, and
722 Fungi. *Protoplasma*. doi:10.1007/S00709-021-01665-7
723 Clare DK, Magescas J, Piolot T, Dumoux M, Vesque C, Pichard E, Dang T, Duvauchelle B,
724 Poirier F, Delacour D. 2014. Basal foot MTOC organizes pillar MTs required for
725 coordination of beating cilia. *Nature communications* **5**:4888. doi:10.1038/ncomms5888
726 Cortés CR, McInerney-Leo AM, Vogel I, Rondón Galeano MC, Leo PJ, Harris JE, Anderson
727 LK, Keith PA, Brown MA, Ramsing M, Duncan EL, Zankl A, Wicking C. 2016.
728 Mutations in human C2CD3 cause skeletal dysplasia and provide new insights into
729 phenotypic and cellular consequences of altered C2CD3 function. *Scientific Reports* **6**.
730 doi:10.1038/srep24083
731 Delgehyr N, Meunier A, Faucourt M, Grau MB, Strehl L, Janke C, Spassky N. 2015.
732 Ependymal cell differentiation, from monociliated to multiciliated cells. *Methods in Cell*
733 *Biology* **127**:19–35. doi:10.1016/bs.mcb.2015.01.004
734 Feldman JL, Geimer S, Marshall WF. 2007. The mother centriole plays an instructive role in
735 defining cell geometry. *PLoS Biol* **5**:e149.
736 Gambarotto D, Zwettler FU, le Guennec M, Schmidt-Cernohorska M, Fortun D, Borgers S,
737 Heine J, Schloetel JG, Reuss M, Unser M, Boyden ES, Sauer M, Hamel V, Guichard P.
738 2019. Imaging cellular ultrastructures using expansion microscopy (U-ExM). *Nature*
739 *Methods* **16**:71–74. doi:10.1038/s41592-018-0238-1
740 Garcia-Gonzalo FR, Reiter JF. 2017. Open Sesame: How Transition Fibers and the Transition
741 Zone Control Ciliary Composition. *Cold Spring Harb Perspect Biol* **9**.
742 doi:10.1101/cshperspect.a028134

743 Geimer S, Melkonian M. 2005. Centrin scaffold in Chlamydomonas reinhardtii revealed by
744 immunoelectron microscopy. *Eukaryot Cell* **4**:1253–1263.
745 Geimer S, Melkonian M. 2004. The ultrastructure of the Chlamydomonas reinhardtii basal
746 apparatus: identification of an early marker of radial asymmetry inherent in the basal
747 body. *J Cell Sci* **117**:2663–2674.
748 Gibson DG, Young L, Chuang RY, Venter JC, Hutchison CA, Smith HO. 2009. Enzymatic
749 assembly of DNA molecules up to several hundred kilobases. *Nature Methods* **6**:343–345.
750 doi:10.1038/nmeth.1318
751 Goodrich L v., Johnson RL, Milenkovic L, McMahon JA, Scott MP. 1996. Conservation of the
752 hedgehog/patched signaling pathway from flies to mice: Induction of a mouse patched
753 gene by Hedgehog. *Genes and Development* **10**:301–312. doi:10.1101/gad.10.3.301
754 Gupta GD, Coyaud É, Gonçalves J, Mojarad BA, Liu Y, Wu Q, Gheiratmand L, Comartin D,
755 Tkach JM, Cheung SWT, Bashkurov M, Hasegan M, Knight JD, Lin ZY, Schueler M,
756 Hildebrandt F, Moffat J, Gingras AC, Raught B, Pelletier L. 2015. A Dynamic Protein
757 Interaction Landscape of the Human Centrosome-Cilium Interface. *Cell* **163**:1484–1499.
758 doi:10.1016/j.cell.2015.10.065
759 Izquierdo D, Wang WJ, Uryu K, Tsou MF. 2014. Stabilization of cartwheel-less centrioles for
760 duplication requires CEP295-mediated centriole-to-centrosome conversion. *Cell Rep*
761 **8**:957–965. doi:10.1016/j.celrep.2014.07.022
762 Kim J, Krishnaswami SR, Gleeson JG. 2008. CEP290 interacts with the centriolar satellite
763 component PCM-1 and is required for Rab8 localization to the primary cilium. *Hum Mol*
764 *Genet* **17**:3796–3805. doi:10.1093/hmg/ddn277
765 Kong D, Sahabandu N, Sullenberger C, Vásquez-Limeta A, Luvsanjav D, Lukasik K, Loncarek
766 J. 2020. Prolonged mitosis results in structurally aberrant and over-elongated centrioles.
767 *The Journal of cell biology* **219**. doi:10.1083/JCB.201910019

768 Kumar D, Reiter J. 2021. How the centriole builds its cilium: of mothers, daughters, and the
769 acquisition of appendages. *Current Opinion in Structural Biology*.
770 doi:10.1016/j.sbi.2020.09.006
771 Le Guennec M, Klena N, Gambarotto D, Laporte MH, Tassin A-M, van den Hoek H, Erdmann
772 PS, Schaffer M, Kovacik L, Borgers S, Goldie KN, Stahlberg H, Bornens M, Azimzadeh
773 J, Engel BD, Hamel V, Guichard P. 2020. A helical inner scaffold provides a structural
774 basis for centriole cohesion. *Science Advances* **6**. doi:10.1126/sciadv.aaz4137
775 Le Guennec M, Klena N, Aeschlimann G, Hamel V, Guichard P. 2021. Overview of the
776 centriole architecture. *Current Opinion in Structural Biology* **66**:58–65.
777 doi:10.1016/j.sbi.2020.09.015
778 Lin J, Heuser T, Song K, Fu X, Nicastro D. 2012. One of the Nine Doublet Microtubules of
779 Eukaryotic Flagella Exhibits Unique and Partially Conserved Structures. *PLoS ONE* **7**.
780 doi:10.1371/journal.pone.0046494
781 Mercey O, al Jord A, Rostaing P, Mahuzier A, Fortoul A, Boudjema AR, Faucourt M, Spassky
782 N, Meunier A. 2019. Dynamics of centriole amplification in centrosome-depleted brain
783 multiciliated progenitors. *Scientific Reports* **9**:1–11. doi:10.1038/s41598-019-49416-2
784 Meunier A, Azimzadeh J. 2016. Multiciliated cells in animals. *Cold Spring Harbor*
785 *Perspectives in Biology* **8**. doi:10.1101/cshperspect.a028233
786 Muto Y, Yoshioka T, Kimura M, Matsunami M, Saya H, Okano Y. 2008. An evolutionarily
787 conserved leucine-rich repeat protein CLERC is a centrosomal protein required for spindle
788 pole integrity. *Cell Cycle* **7**:2738–2748.
789 Nachury M v. 2018. The molecular machines that traffic signaling receptors into and out of
790 cilia. *Current Opinion in Cell Biology*. doi:10.1016/j.ceb.2018.03.004

Nommick A, Boutin C, Rosnet O, Schirmer C, Bazellières E, Thomé V, Loiseau E, Viallat A, Kodjabachian L. 2022. Lrrcc1 and Ccdc61 are conserved effectors of multiciliated cell function. *Journal of cell science*. doi:10.1242/JCS.258960

Ooi J. 2015. Mutations in C2CD3 cause oral-facial-digital syndrome through deregulation of centriole length. *Clinical Genetics* **87**:328–329. doi:10.1111/cge.12545

Reiter JF, Leroux MR. 2017. Genes and molecular pathways underpinning ciliopathies. *Nat Rev Mol Cell Biol* **18**:533–547. doi:10.1038/nrm.2017.60

Rohatgi R, Milenkovic L, Scott MP. 2007. Patched1 regulates hedgehog signaling at the primary cilium. *Science* **317**:372–376. doi:10.1126/science.1139740

Romani M, Micalizzi A, Valente EM. 2013. Joubert syndrome: congenital cerebellar ataxia with the molar tooth. *Lancet neurology* **12**:894–905. doi:10.1016/S1474-4422(13)70136-4

Schneiter M, Halm S, Odriozola A, Mogel H, Rička J, Stoffel MH, Zuber B, Frenz M, Tschanz SA. 2021. Multi-scale alignment of respiratory cilia and its relation to mucociliary function. *Journal of Structural Biology* **213**:107680. doi:10.1016/j.jsb.2020.107680

Shaheen R, Szymanska K, Basu B, Patel N, Ewida N, Faqeih E, al Hashem A, Derar N, Alsharif H, Aldahmesh MA, Alazami AM, Hashem M, Ibrahim N, Abdulwahab FM, Sonbul R, Alkuraya H, Alnemer M, al Tala S, Al-Husain M, Morsy H, Seidahmed MZ, Meriki N, Al-Owain M, AlShahwan S, Tabarki B, Salih MA, Ciliopathy W, Faquih T, El-Kalioby M, Ueffing M, Boldt K, Logan C v, Parry DA, al Tassan N, Monies D, Megarbane A, Abouelhoda M, Halees A, Johnson CA, Alkuraya FS. 2016. Characterizing the morbid genome of ciliopathies. *Genome biology* **17**:242. doi:10.1186/s13059-016-1099-5

Sharma A, Olieric N, Steinmetz MO. 2021. Centriole length control. *Current Opinion in Structural Biology* **66**:89–95. doi:10.1016/j.sbi.2020.10.011

815 Silflow CD, LaVoie M, Tam LW, Tousey S, Sanders M, Wu W, Borodovsky M, Lefebvre PA.
816 2001. The Vfl1 Protein in Chlamydomonas localizes in a rotationally asymmetric pattern
817 at the distal ends of the basal bodies. *J Cell Biol* **153**:63–74.
818 Singla V, Romaguera-Ros M, Garcia-Verdugo JM, Reiter JF. 2010. Ofd1, a human disease
819 gene, regulates the length and distal structure of centrioles. *Dev Cell* **18**:410–424.
820 Sofroniew N, Lambert T, Evans K, Nunez-Iglesias J, Yamauchi K, Solak AC, Bokota G,
821 ziyangczi, Buckley G, Winston P, Tung T, Pop DD, Hector, Freeman J, Bussonnier M,
822 Boone P, Royer L, Har-Gil H, Axelrod S, Rokem A, Bryant, Kiggins J, Huang M, Vemuri
823 P, Dunham R, Manz T, jakirkham, Wood C, Siqueira A de, Chopra B. 2020. napari/napari:
824 0.3.8rc1. doi:10.5281/ZENODO.4046812
825 Takao D, Yamamoto S, Kitagawa D. 2019. A theory of centriole duplication based on self-
826 organized spatial pattern formation. *Journal of Cell Biology* **218**:3537–3547.
827 doi:10.1083/JCB.201904156
828 Thauvin-Robinet C, Lee JS, Lopez E, Herranz-Pérez V, Shida T, Franco B, Jego L, Ye F,
829 Pasquier L, Loget P, Gigot N, Aral B, Lopes CAM, St-Onge J, Bruel AL, Thevenon J,
830 González-Granero S, Alby C, Munnich A, Vekemans M, Huet F, Fry AM, Saunier S,
831 Rivière JB, Attié-Bitach T, Garcia-Verdugo JM, Faivre L, Mégarbané A, Nachury M v.
832 2014. The oral-facial-digital syndrome gene C2CD3 encodes a positive regulator of
833 centriole elongation. *Nature Genetics* **46**:905–911. doi:10.1038/ng.3031
834 Tsai JJ, Hsu W bin, Liu JH, Chang CW, Tang TK. 2019. CEP120 interacts with C2CD3 and
835 Talpid3 and is required for centriole appendage assembly and ciliogenesis. *Scientific*
836 *Reports* **9**. doi:10.1038/s41598-019-42577-0
837 Vaughan S, Gull K. 2016. Basal body structure and cell cycle-dependent biogenesis in
838 Trypanosoma brucei. *Cilia*. doi:10.1186/s13630-016-0023-7

839 Vorobjev IA, Chentsov YS. 1980. The ultrastructure of centriole in mammalian tissue culture
840 cells. *Cell biology international reports* **4**:1037–1044. doi:10.1016/0309-1651(80)90177-
841 0
842 Wang Lei, Failler M, Fu W, Dynlacht BD. 2018. A distal centriolar protein network controls
843 organelle maturation and asymmetry. *Nature Communications* **9**. doi:10.1038/s41467-
844 018-06286-y
845 Wang L, Failler M, Fu W, Dynlacht BD. 2018. A distal centriolar protein network controls
846 organelle maturation and asymmetry. *Nature communications* **9**:3938.
847 doi:10.1038/s41467-018-06286-y
848 Yamamoto S, Kitagawa D. 2021. Emerging insights into symmetry breaking in centriole
849 duplication: updated view on centriole duplication theory. *Current Opinion in Structural*
850 *Biology*. doi:10.1016/j.sbi.2020.08.005
851 Yang TT, Chong WM, Wang WJ, Mazo G, Tanos B, Chen Z, Tran TMN, Chen Y de, Weng
852 RR, Huang CE, Jane WN, Tsou MFB, Liao JC. 2018. Super-resolution architecture of
853 mammalian centriole distal appendages reveals distinct blade and matrix functional
854 components. *Nature Communications* **9**:1–11. doi:10.1038/s41467-018-04469-1
855 Ye X, Zeng H, Ning G, Reiter JF, Liu A. 2014. C2cd3 is critical for centriolar distal appendage
856 assembly and ciliary vesicle docking in mammals. *Proceedings of the National Academy*
857 *of Sciences of the United States of America* **111**:2164–2169.
858 doi:10.1073/pnas.1318737111
859 Yubuki N, Leander BS. 2013. Evolution of microtubule organizing centers across the tree of
860 eukaryotes. *The Plant journal : for cell and molecular biology* **75**:230–244.
861 doi:10.1111/tpj.12145

862 Zhang D, Aravind L. 2012. Novel transglutaminase-like peptidase and C2 domains elucidate
863 the structure, biogenesis and evolution of the ciliary compartment. *Cell Cycle* **11**:3861–
864 3875. doi:10.4161/cc.22068

865

866

867 **Figure legends**

868

869 **Figure 1. LRRCC1 is localized in a rotationally asymmetric manner at the distal end of**
870 **centrioles in the human centrosome. a)** LRRCC1 localization in non-treated RPE1 cells
871 (left) or in cells treated with nocodazole to disperse the pericentriolar satellites (right).
872 LRRCC1 (Ab2, yellow), γ-tubulin (PCM, magenta) and DNA (cyan). Bar, 5 µm (insets, 2 µm).
873 **b)** Longitudinal view of centrioles and procentrioles in the duplicating centrosome of an RPE1
874 cell analyzed by U-ExM. LRRCC1 (Ab2, yellow), acetylated tubulin (magenta). Bar, 0.5 µm.
875 **c)** Centrioles from WT RPE1 cells as seen from the distal end. LRRCC1 (Ab2, yellow),
876 acetylated tubulin (magenta). Images are maximum intensity projections of individual z-
877 sections encompassing the LRRCC1 signal. Note that an apparent shift between channels
878 occurs when centrioles are slightly angled with respect to the imaging axis. Bar, 0.2 µm. **d)**
879 Lateral distance between LRRCC1 (left, yellow) or hPOC5 (middle, cyan) signal intensity
880 peaks and the centriole center (given by the position of acetylated tubulin intensity peak,
881 magenta) in ciliated RPE1 cells. Individual intensity profiles were measured along the green
882 lines. The approximate position of the centriole is shown (white cylinders). Note that LRRCC1
883 and hPOC5 were also detected at the periphery of the centriole. Right: interpeak distance (d).
884 Bars, mean ± SD, 31 cells from 2 different experiments (Kolmogorov-Smirnov test). **e)**
885 Workflow for calculating the average staining from 3D-reconstructed individual centrioles
886 generated from confocal z-stacks. The brightest part of LRRCC1 signal was used as a reference
887 point to align the centrioles. **f)** Average LRRCC1 staining obtained from 34 individual
888 centrioles viewed from the distal end, in transverse and longitudinal views. A diagram
889 representing the average pattern in transverse view is also shown.

890

891 **Figure 2. The LRRCC1 rotationally asymmetric pattern is conserved in mouse MCCs.**
892 **a)** Centrioles in the cytoplasm of mouse ependymal cells differentiating *in vitro* analyzed by
893 U-ExM, in longitudinal and transverse view. Lrrcc1 (Ab2, yellow), γ-tubulin (basal foot cap,
894 cyan) and acetylated tubulin (magenta). Of note, γ-tubulin was also detected in the proximal
895 lumen of centrioles. Bar, 0.2 µm. **b)** Procentrioles assembling via the centriolar (right) or the
896 deuterosome pathway (left and center) in ependymal cells. Lrrcc1 (Ab2, yellow), acetylated
897 tubulin (magenta). Bar, 0.2 µm. **c)** Transverse view of centrioles docked at the apical membrane
898 in fully differentiated mouse tracheal cells, viewed from the distal end. Lrrcc1 (Ab2, yellow),
899 γ-tubulin (cyan) and acetylated tubulin (magenta). Bar, 0.2 µm. **d)** Average image generated
900 from 35 individual centrioles from mouse trachea, viewed from the distal end, shown in
901 transverse and longitudinal views. The position of the basal foot (cyan dotted line) stained with
902 γ-tubulin was used as a reference point to align the centrioles. A diagram of the average pattern
903 in transverse view is shown, in which the direction of ciliary beat (Schneiter et al., 2021) is
904 represented by a dotted arrow and the basal foot axis by a green line. Triplets are numbered
905 counterclockwise from the LRRCC1 signal.
906
907 **Figure 3. Procentriole assembly site is partly correlated with centriole rotational polarity.**
908 **a)** Diagram showing the localization of Vfl1p (cyan) in the centrioles/basal bodies (grey) and
909 procentrioles/probasal bodies (pink) of *C. reinhardtii*. The microtubule roots are also shown.
910 **b)** Early stage of procentriole assembly stained for LRRCC1 (Ab2, cyan), SAS-6 (yellow) and
911 acetylated tubulin (magenta) in a HEK 293 cell. The brightness of the acetylated tubulin
912 labeling was increased in the inserts. Bar, 0.1 µm. **c)** Successive stages of centriole elongation
913 in HEK 293 cells stained for LRRCC1 (Ab2, cyan) and acetylated tubulin (magenta). Bar, 0.1
914 µm. **d)** Location of LRRCC1 in the procentrioles (top panels) and position of the procentriole
915 relative to its parent centriole polarity (bottom panels), in RPE1 and HEK 293 centrioles

916 analyzed by U-ExM. For each diplosome, the angle between LRRCC1 in the procentriole and
917 the centriole long axis (top panels), or between the procentriole and LRRCC1 in the centriole
918 (bottom panels) was measured. The number of diplosomes analyzed is indicated. p values are
919 indicated when statistically different from a random distribution (χ^2-test).
920
921 **Figure 4. LRRCC1 is required for ciliary assembly and signaling. a)** Left: LRRCC1
922 staining (Ab2) of WT or LRRCC1-defficient RPE1 cells obtained by CRISPR/Cas9 editing
923 (clones 1.1, 1.2 and 1.9). Bar, 2 µm. Right: quantification of fluorescence intensity in WT or
924 CRISPR clones treated with control or LRRCC1 siRNAs. Bars, mean ± SD, 3 independent
925 experiments. p values are provided when statistically significant from the corresponding
926 control (One-way ANOVA). **b)** Quantification of LRRCC1 distal pool at the mother centriole
927 of ciliated WT or CRISPR cells. Left: Airyscan images showing the region of interest (circled).
928 LRRCC1 (yellow), acetylated tubulin (magenta). Bar: 0.5 µm. Right: quantification of the
929 corresponding signal. Bars, mean ± SD, ≥ 47 cells from 2 independent experiments. p values
930 are provided when statistically significant from the corresponding control (One-way ANOVA).
931 **c)** Percentage of ciliated cells in WT or CRISPR cells treated with control or LRRCC1 siRNAs
932 and serum-deprived during 24 hours. Bars, mean ± SD, ≥ 204 cells from 3 independent
933 experiments for each condition. p values are provided when statistically significant from the
934 corresponding control (One-way ANOVA). **d)** Left: SMO (yellow) accumulation at primary
935 cilia (ARL13B, magenta) following SAG-induction of the Hedgehog pathway, in WT or
936 CRISPR cells. Bar, 2 µm. Right: quantification of ciliary SMO expressed as a percentage of
937 the SAG-treated WT mean. Bars, mean ± SD, 3 independent experiments. p values are provided
938 when statistically significant from the corresponding control (One-way ANOVA). **e)** Ciliary
939 SMO expressed as a percentage of the SAG-induced control mean in RPE1 cells treated with

940 control or LRRCC1 siRNAs. Bars, mean ± SD, 3 independent experiments. p values are
941 provided when statistically significant from the corresponding control (One-way ANOVA).
942
943 **Figure 5. Depleting LRRCC1 induces defects in centriole structure. a)** Centriole length in
944 mother (MC) and daughter (DC) centrioles analyzed by U-ExM in WT or LRRCC1-deficient
945 clones (1.1 and 1.9). Left: Centrioles were stained for acetylated tubulin (magenta) and CEP164
946 (yellow) to measure centriole length (arrows). Bar, 0.5 µm. Right: Quantification. Bars, mean
947 ± SD, ≥ 38 centrioles from 3 independent experiments. p values are provided when statistically
948 significant from the corresponding control (One-way ANOVA). **b)** Centriole length in control
949 cells or CRISPR cells treated with LRRCC1 siRNA-1 and stained for acetylated tubulin and
950 CEP83. Bars, mean ± SD, ≥ 43 centrioles from 3 independent experiments. p values are
951 provided when statistically significant from the corresponding control (One-way ANOVA). **c)**
952 Transmission electron microscopy view of centrioles in WT and CRISPR (clone 1.9) RPE1
953 cells. Note that the 1.9 centrioles are from the same cell. N = 9 centrioles from 8 different cells
954 for clone 1.9, 3 centrioles from 2 different cells for WT. Bar, 0.5 µm. **d)** Examples of normal
955 DAs, DAs with abnormal morphology (white arrowhead: abnormal spacing between
956 consecutive DAs; cyan arrowhead: abnormal DA shape) or missing DAs (grey arrowhead) in
957 RPE1 cells stained with CEP164 (yellow) and analyzed by U-ExM. Images are maximum
958 intensity projections of individual z-sections encompassing the CEP164 signal. Note that an
959 apparent shift between channels occurs when centrioles are slightly angled with respect to the
960 imaging axis. Bar, 1 µm. **e)** Percentages of centrioles presenting anomalies in CEP164 staining
961 in WT or CRISPR RPE1 cells. ≥ 87 centrioles from 8 independent experiments for each
962 condition. p values are provided when statistically significant from the corresponding control
963 (Two-way ANOVA). **f)** Percentages of centrioles presenting anomalies in CEP164 staining in
964 WT or CRISPR HEK 293 (clone 25) cells. ≥ 40 centrioles from 4 independent experiments for

965 each condition. p values are provided when statistically significant from the corresponding
966 control (Two-way ANOVA). **g)** Examples of normal DAs, DAs with abnormal morphology
967 (white arrowhead) or missing DAs (grey arrowhead) in RPE1 cells stained with CEP83
968 (yellow) and analyzed by U-ExM. Images are maximum intensity projections of individual z-
969 sections encompassing the CEP83 signal. Note that apparent shift between channels and
970 decreased circularity occur when centrioles are slightly angled with respect to the imaging axis.
971 Bar, 1 µm. **h)** Percentages of centrioles presenting anomalies in CEP83 staining in WT RPE1
972 cells and CRISPR clones with or without RNAi treatment. ≥ 56 centrioles from 3 independent
973 experiments for each condition. p values are provided when statistically significant from the
974 corresponding control (Two-way ANOVA).
975
976 **Figure 6. C2CD3 localizes asymmetrically at the distal end of centrioles and is affected**
977 **by LRRCC1-depletion. a)** C2CD3 levels at the centrosome of WT or CRISPR RPE1 cells.
978 Bars, mean ± SD, 3 independent experiments. p values are provided when statistically
979 significant from the corresponding control (One-way ANOVA). **b)** C2CD3 levels at the
980 centrosome in RPE1 cells treated with control or LRRCC1 siRNAs. Bars, mean ± SD, 3
981 independent experiments. p values are provided when statistically significant from the
982 corresponding control (One-way ANOVA). **c)** Longitudinal view of a centriole analyzed by U-
983 ExM and stained for C2CD3 (yellow) and acetylated tubulin (magenta). Bar, 0.2 µm. **d)**
984 Centrioles from WT RPE1 cells as viewed from the distal end. C2CD3 (yellow), acetylated
985 tubulin (magenta). Images are maximum intensity projections of individual z-sections
986 encompassing the C2CD3 signal. Note that an apparent shift between channels occurs when
987 centrioles are slightly angled with respect to the imaging axis. Bar, 0.2 µm. **e)** Average C2CD3
988 images obtained from 33 individual centrioles from WT RPE1 cells viewed from the distal end,
989 in transverse views. One end of the C-pattern was used as a reference point to align individual

990 centrioles. **f)** Centrioles from untreated CRISPR cells or CRISPR cells treated with LRRCC1
991 RNAi in transverse section as viewed from the distal end. C2CD3 (yellow), acetylated tubulin
992 (magenta). Images are maximum intensity projections of individual z-sections encompassing
993 the C2CD3 signal. Note that an apparent shift between channels occurs when centrioles are
994 slightly angled with respect to the imaging axis. Bar, 0.2 µm. **g)** Average C2CD3 images
995 obtained from untreated or RNAi-treated CRISPR cells viewed from the distal end, in
996 transverse views. The number or individual centrioles used for generating each average is
997 indicated.
998
999 **Figure 7. C2CD3 and LRRCC1 partially colocalize at the distal end of centrioles. a)** RPE1
1000 centrioles processed for U-ExM and stained for LRRCC1 (Ab2, yellow), C2CD3 (cyan) and
1001 acetylated tubulin (magenta). Bar, 0.1 µm. **b)** Model showing the possible location of LRRCC1
1002 and C2CD3 relative to each other within human centrioles. Right panel: diagram showing the
1003 respective positions of the acorn (Geimer and Melkonian, 2004) and Vfl1p (Silflow et al., 2001)
1004 in *C. reinhardtii*. The direction of the flagellar beat is indicated by a dotted arrow, and the distal
1005 striated fiber is in grey. **c)** Evolution of the roles played by Vfl1p/LRRCC1 proteins and
1006 associated rotationally asymmetric centriolar substructures. In *C. reinhardtii*, Vfl1p is required
1007 for proper ciliary assembly (1), as well as for the formation of fibers and microtubular roots (2)
1008 that control the position of centrioles and procentrioles (3), and overall cellular organization
1009 (Adams et al., 1985; Silflow et al., 2001). In human cells, LRRCC1 and C2CD3 are required
1010 for primary cilium assembly (1) - this study and (Thauvin-Robinet et al., 2014; Ye et al., 2014)
1011 - and a role in asymmetric anchoring of cytoskeletal elements to the centriole may also be
1012 conserved (2), which could indirectly affect the determination of procentriole assembly site.
1013
1014

1015 **Supplemental material**

1016 **Fig. S1** provides additional data on LRRCC1 expression in CRISPR clones and RNAi-treated
1017 cells. **Fig. S2** presents the image analysis pipeline for generating the average images of
1018 LRRCC1 and C2CD3 staining. **Fig. S3** shows the genomic deletions in the CRISPR clone 1.1
1019 and the corresponding transcripts. **Fig. S4** shows the quantification of the DA component
1020 CEP164, and the distal centriole components CEP290 and OFD1, at the centrosome of RPE1
1021 cells depleted from LRRCC1 by CRISPR or RNAi. **Fig. S5** shows that C2CD3 is not co-
1022 immunoprecipitated with GFP-LRRCC1.

Gaudin *et al.*

Figure 1

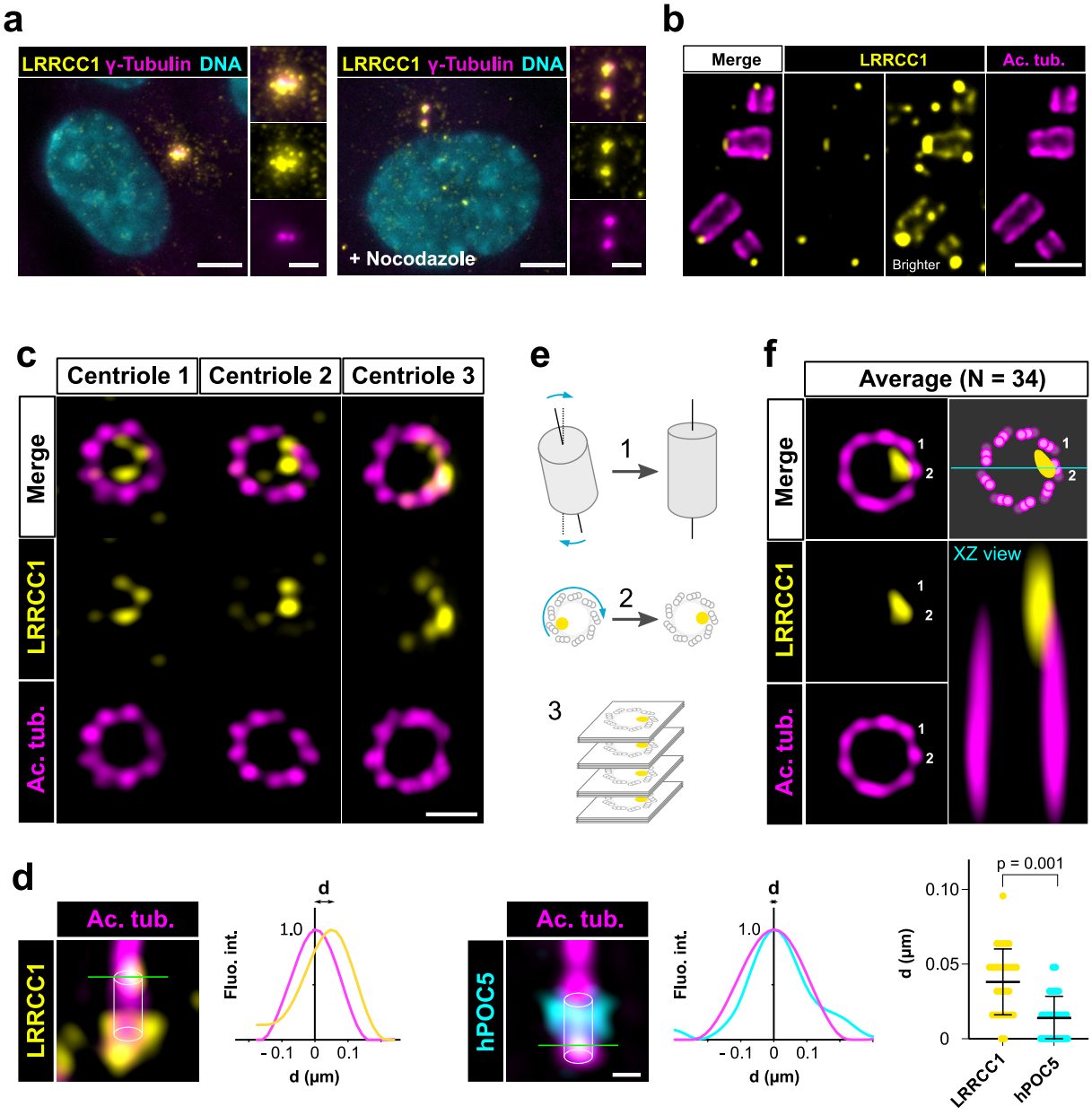

Figure 2

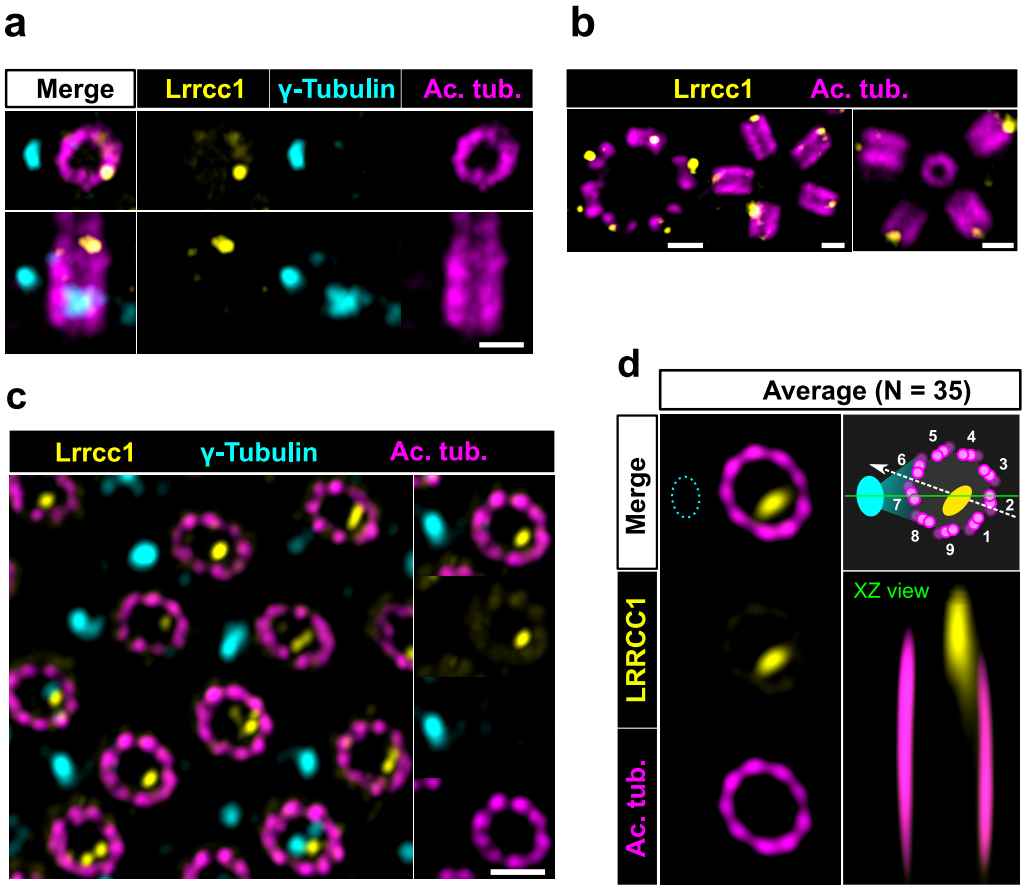
a
Merge
Lrrcc1
γ-Tubulin
Ac. tub.
b
Lrrcc1
Ac. tub.
c
Lrrcc1
γ-Tubulin
Ac. tub.
d
Average (N = 35)
Merge
LRRCC1
Ac. tub.
5
4
6
3
7
2
8
1
9
XZ view

Figure 3

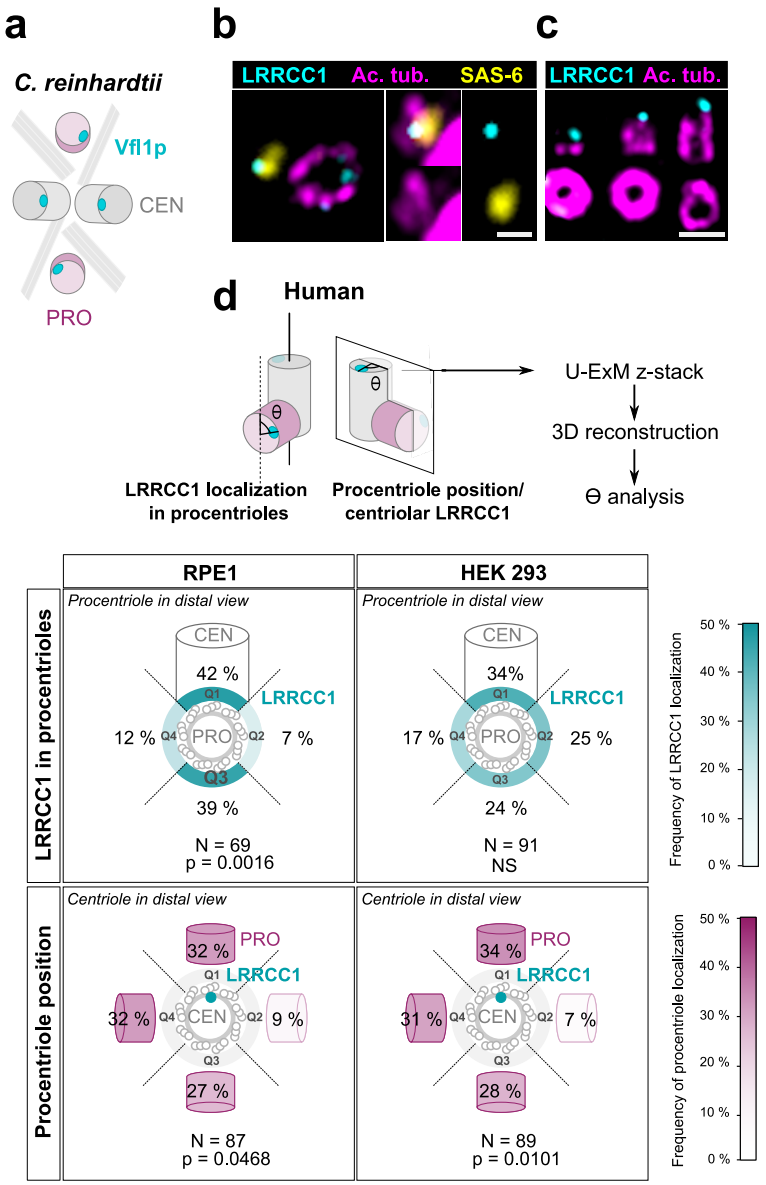
a
C. reinhardtii
Vfl1p
CEN
PRO
b
LRRCC1 Ac. tub. SAS-6
c
LRRCC1 Ac. tub.
d
Human
θ
U-ExM z-stack
3D reconstruction
Θ analysis
LRRCC1 localization in procentrioles
Procentriole position/ centriolar LRRCC1
RPE1
HEK 293
LRRCC1 in procentrioles
Procentriole in distal view
CEN
42 %
LRRCC1
12 %
PRO
7 %
39 %
N = 69
p = 0.0016
34%
17 %
25 %
24 %
N = 91
NS
Frequency of LRRCC1 localization
50 %
40 %
30 %
20 %
10 %
0 %
Procentriole position
Centriole in distal view
32 %
PRO
9 %
27 %
N = 87
p = 0.0468
34 %
31 %
7 %
28 %
N = 89
p = 0.0101
Frequency of procentriole localization
Q1
Q2
Q3
Q4

Figure 4

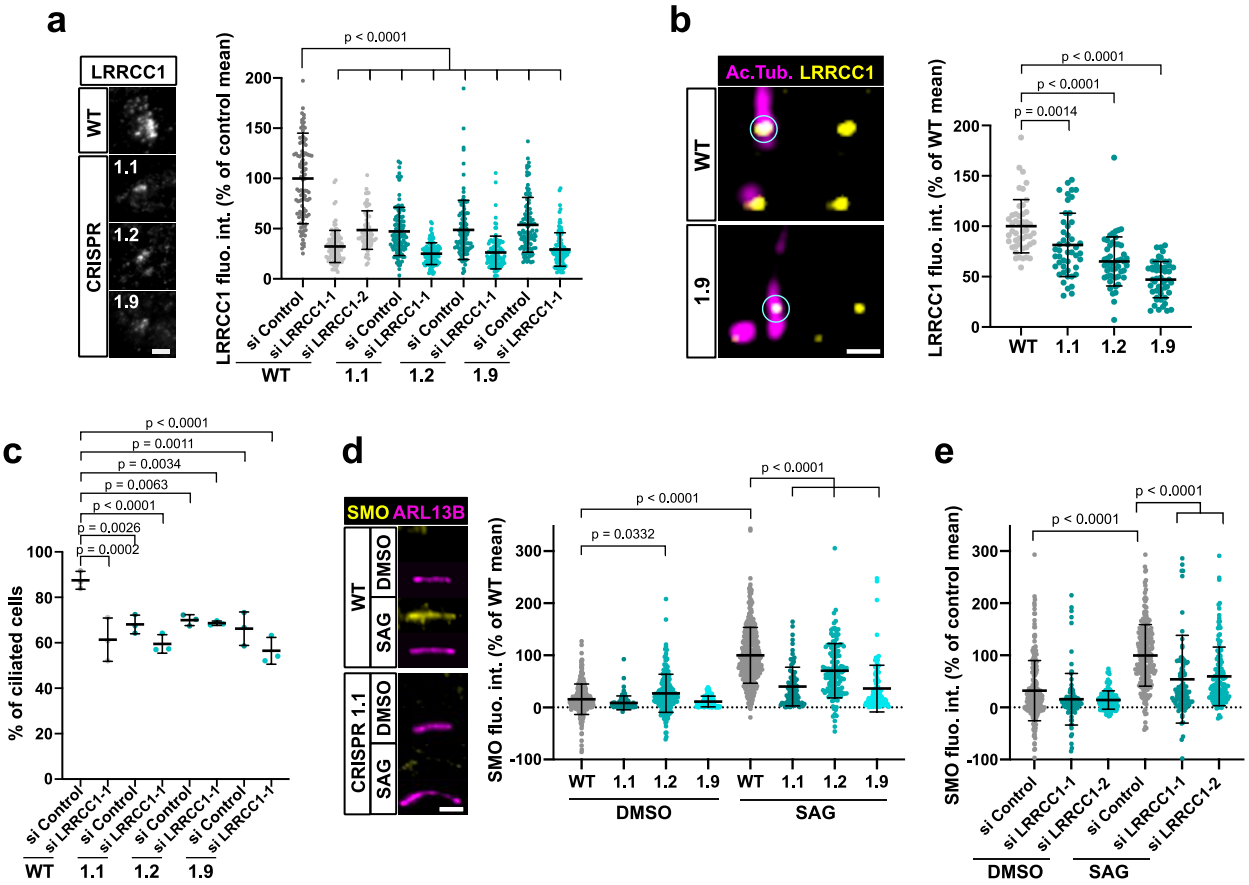
a
LRRCC1
WT
CRISPR
1.1
1.2
1.9
LRRCC1 fluo. int. (% of control mean)
p < 0.0001
si Control
si LRRCC1-1
si LRRCC1-2
WT
1.1
1.2
1.9
b
Ac.Tub. LRRCC1
WT
1.9
LRRCC1 fluo. int. (% of WT mean)
p < 0.0001
p < 0.0001
p = 0.0014
c
% of ciliated cells
p < 0.0001
p = 0.0011
p = 0.0034
p = 0.0063
p < 0.0001
p = 0.0026
p = 0.0002
d
SMO ARL13B
WT
DMSO
SAG
CRISPR 1.1
SMO fluo. int. (% of WT mean)
p < 0.0001
p = 0.0332
p < 0.0001
DMSO
SAG
e
SMO fluo. int. (% of control mean)
p < 0.0001
p < 0.0001
si LRRCC1-2

Figure 5

Gaudin *et al.*

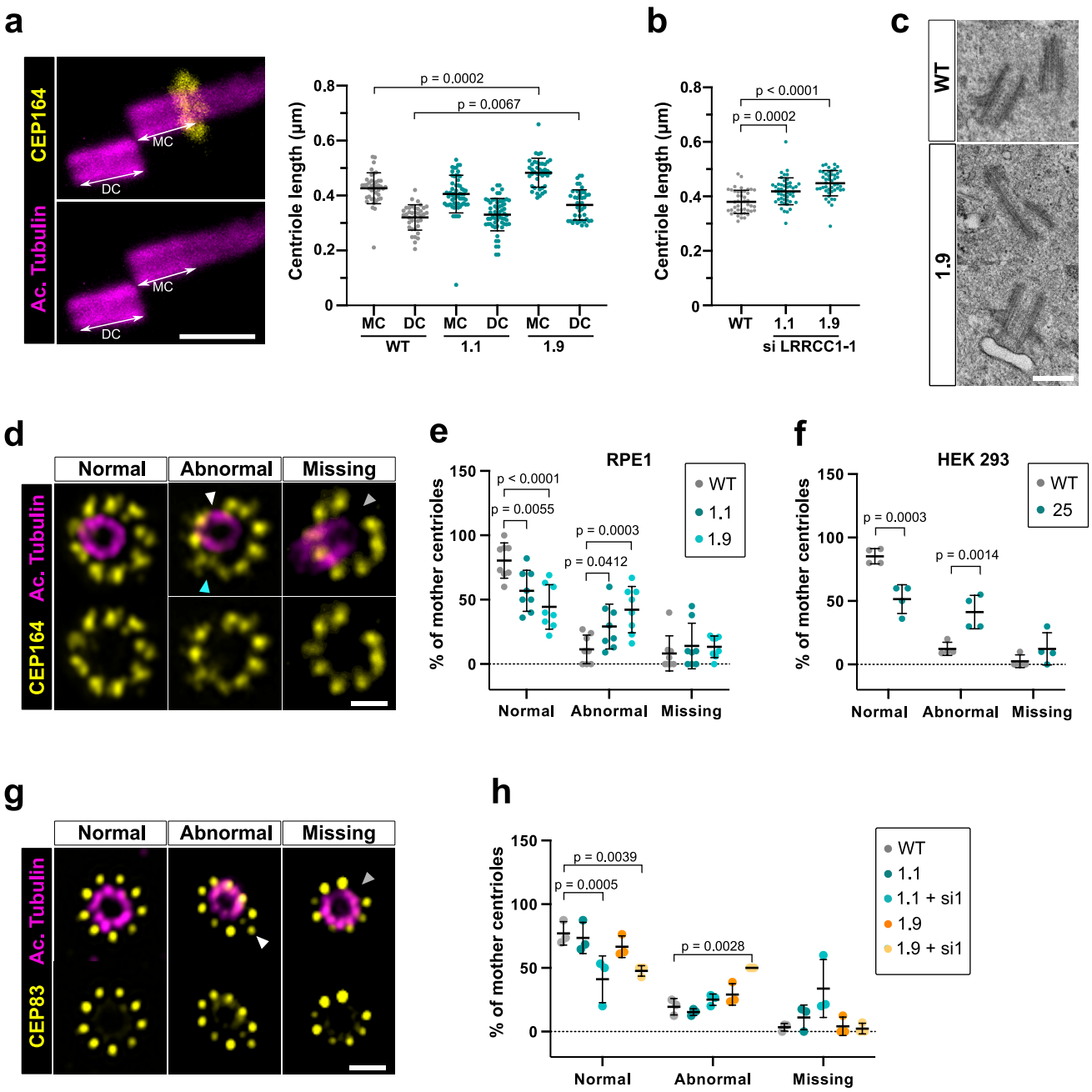

Figure 6

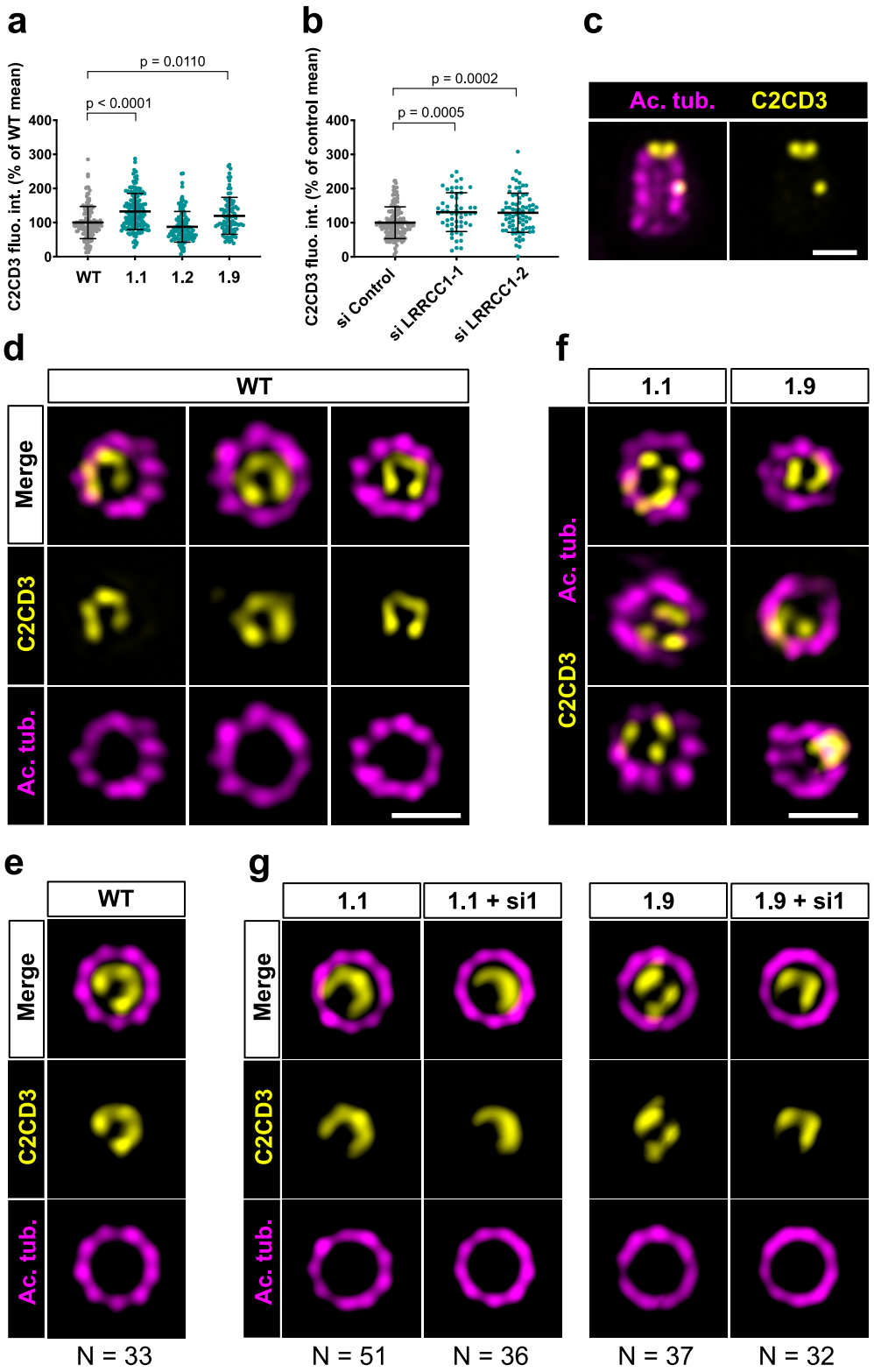
a
C2CD3 fluo. int. (% of WT mean)
p = 0.0110
p < 0.0001
400
300
200
100
0
WT
1.1
1.2
1.9
b
C2CD3 fluo. int. (% of control mean)
p = 0.0002
p = 0.0005
si Control
si LRRCC1-1
si LRRCC1-2
c
Ac. tub.
C2CD3
d
WT
Merge
C2CD3
Ac. tub.
f
1.1
1.9
Ac. tub.
C2CD3
e
WT
Merge
C2CD3
Ac. tub.
g
1.1
1.1 + si1
1.9
1.9 + si1
Merge
C2CD3
Ac. tub.
N = 33
N = 51
N = 36
N = 37
N = 32

Figure 7

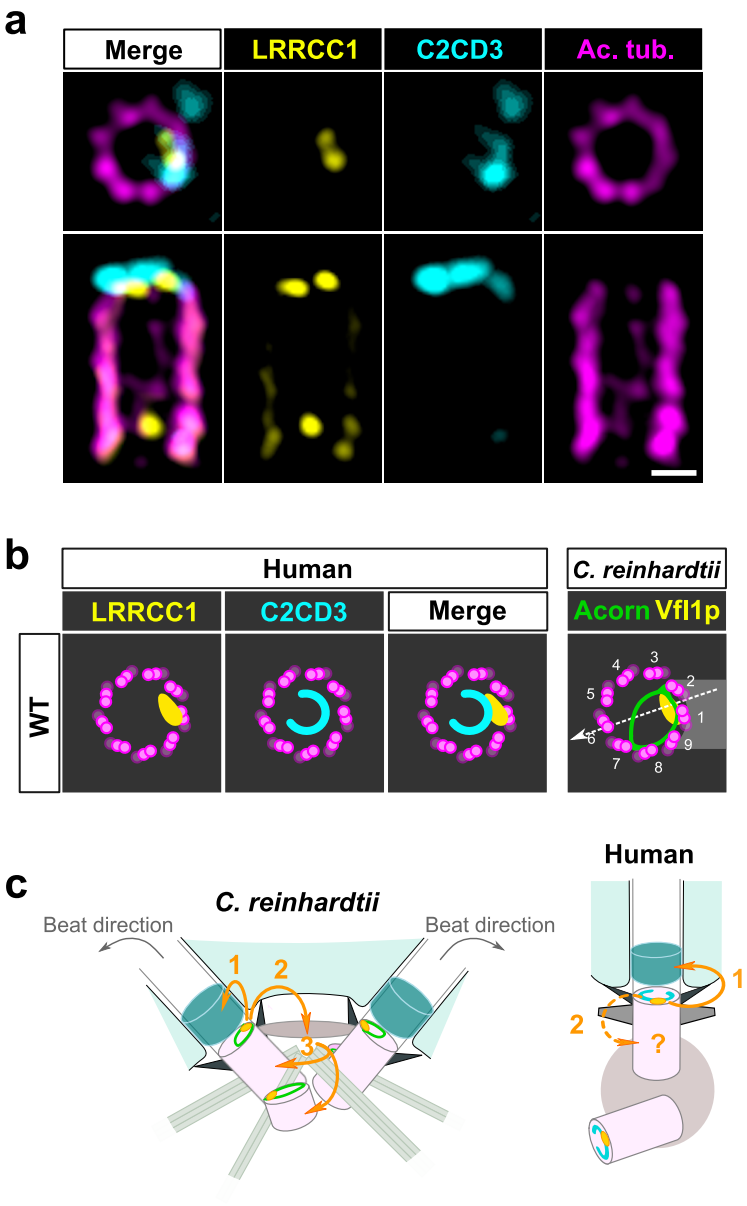
a
Merge
LRRCC1
C2CD3
Ac. tub.
b
Human
C. reinhardtii
LRRCC1
C2CD3
Merge
Acorn
Vfl1p
WT
1
2
3
4
5
6
7
8
9
c
C. reinhardtii
Beat direction
Beat direction
1
2
3
Human
1
2
?